

Article

Similarities and Improvements of GPM Dual-Frequency Precipitation Radar (DPR) upon TRMM Precipitation Radar (PR) in Global Precipitation Rate Estimation, Type Classification and Vertical Profiling

Jinyu Gao ¹, Guoqiang Tang ¹  and Yang Hong ^{1,2,*}

¹ State Key Laboratory of Hydrosience and Engineering, Department of Hydraulic Engineering, Tsinghua University, Beijing 100084, China; gaojy17@mails.tsinghua.edu.cn (J.G.); tgq14@mails.tsinghua.edu.cn (G.T.)

² Department of Civil Engineering and Environmental Science, University of Oklahoma, Norman, OK 73019, USA

* Correspondence: hongyang@tsinghua.edu.cn; Tel.: +86-10-6278-7394

Received: 20 August 2017; Accepted: 2 November 2017; Published: 7 November 2017

Abstract: Spaceborne precipitation radars are powerful tools used to acquire adequate and high-quality precipitation estimates with high spatial resolution for a variety of applications in hydrological research. The Global Precipitation Measurement (GPM) mission, which deployed the first spaceborne Ka- and Ku-dual frequency radar (DPR), was launched in February 2014 as the upgraded successor of the Tropical Rainfall Measuring Mission (TRMM). This study matches the swath data of TRMM PR and GPM DPR Level 2 products during their overlapping periods at the global scale to investigate their similarities and DPR's improvements concerning precipitation amount estimation and type classification of GPM DPR over TRMM PR. Results show that PR and DPR agree very well with each other in the global distribution of precipitation, while DPR improves the detectability of precipitation events significantly, particularly for light precipitation. The occurrences of total precipitation and the light precipitation (rain rates < 1 mm/h) detected by GPM DPR are ~1.7 and ~2.53 times more than that of PR. With regard to type classification, the dual-frequency (Ka/Ku) and single frequency (Ku) methods performed similarly. In both inner (the central 25 beams) and outer swaths (1–12 beams and 38–49 beams) of DPR, the results are consistent. GPM DPR improves precipitation type classification remarkably, reducing the misclassification of clouds and noise signals as precipitation type “other” from 10.14% of TRMM PR to 0.5%. Generally, GPM DPR exhibits the same type division for around 82.89% (71.02%) of stratiform (convective) precipitation events recognized by TRMM PR. With regard to the freezing level height and bright band (BB) height, both radars correspond with each other very well, contributing to the consistency in stratiform precipitation classification. Both heights show clear latitudinal dependence. Results in this study shall contribute to future development of spaceborne radar precipitation retrievals and benefit hydrological and meteorological research.

Keywords: TRMM PR; GPM DPR; precipitation; rain type; global comparison

1. Introduction

Precipitation plays a key role in the water cycle, which is of vital importance for life on Earth [1,2]. However, obtaining accurate and sufficient precipitation estimates remains a huge challenge because of the high spatial and temporal variability of precipitation. Rain gauges and ground-based radars often suffer from sparse distribution and limited spatial coverage [3–5]. These shortcomings directly

lead to the prosperity of satellite-based precipitation products. Although satellite-based infrared (IR)/visible (VIS) data have high temporal sampling frequencies, the relationship between the received radiance from cloud and surface rainfall is indirect. This, in addition to the fact that information regarding rain rates beneath precipitating clouds is insufficient, results in the unsatisfying precipitation estimates [6]. Passive microwave (PMW) methods generally provide more reliable estimates of instantaneous precipitation and can be used for snowfall detection and rain type classification [2,7,8]. Nevertheless, PMW techniques suffer from extremely low spatial (>10 km) and temporal resolution, due to their platforms in low earth orbits. Compared to abovementioned sensors, spaceborne radars, which emit and receive active microwave signals, are able to offer the most precise and detailed information about precipitation and its three-dimensional structure [9,10].

Since its launch in 1997, the Tropical Rainfall Measuring Mission (TRMM) satellite, focusing on measuring medium to heavy rainfall over the tropical and subtropical regions, has provided precipitation observation data for more than 17 years. On 8 April 2015, the TRMM satellite stopped collecting data, officially ceasing operation in June 2015. The precipitation radar (PR) onboard the TRMM satellite was the first spaceborne radar that aimed to provide three-dimensional maps of storm structure and yielded valuable information about rain intensity and distribution. In February 2014, the National Aeronautics and Space Administration (NASA) and the Japan Aerospace Exploration Agency (JAXA) launched Global Precipitation Mission (GPM) Core Observatory. As the successor of the TRMM satellite, the GPM satellite carries the first spaceborne dual-frequency precipitation radar (DPR) [5]. In addition to the Ku-band radar, which operates at 13.6 GHz and is also applied in PR, the Ka-band radar of GPM DPR is more adept at capturing light rain, at a higher frequency of 35.5 GHz [11].

The evaluation of the performance of spaceborne radars has always been a hot topic and several previous studies have been carried out for TRMM PR [12–16]. The comparison between TRMM PR and ground-based precipitation estimates suggests that generally TRMM performs quite well [12,17,18] when the signal attenuation is not severer, and particularly TRMM PR measurements can achieve an agreement of ~1 dB with ground radar observations in Texas and Florida [19]. By comparing TRMM PR latest version 7 products with the NEXRAD-based Q2, it is discovered that the bias of rain rate estimates from V7 has been improved from an underestimation bias of –23% (from V6) to –18% [20]. However, TRMM PR tends to underestimate heavy precipitation around the tropical rainfall maximum, according to [15,21], leading to the underestimation of near-surface precipitation water content. By comparing with the ground-based Weather Surveillance Radar-1988 Doppler (WSR) at Melbourne, Florida, Liao et al. [22] discovered that TRMM PR correlates well for stratiform rain, while for convective rain, overestimate light rain and underestimate moderate to heavy rain. Moreover, given its quasi-global consistence, some studies have revealed TRMM PR's potential in systematic monitoring and correcting ground radar biases [18,23–25].

Awaka et al. [26] indicated that the detected bright band (BB) number of TRMM PR strongly depends on the antenna scan angle and the BB is detected in only about 40% of stratiform rain events. Hamada et al. [27] used eleven-year records of TRMM PR to demonstrate that the most extreme rainfall events are more closely related to less intense convection [26]. They further investigated the impacts of the detectability enhancement of GPM DPR over TRMM PR using six months of observation, finding that both the occurrence and volume of overall precipitation increased by ~21.1% and ~1.9%, respectively [28]. TRMM PR and GPM DPR correspond reasonably well with each other based on a global intercomparison, although GPM DPR significantly improved the detection of light precipitation and the sampling rate of snowfall estimation according to [29]. Furthermore, both radars exhibit satisfying correlation with in situ observations from Mainland China [29].

However, because of the relatively short operation period of GPM, studies concerning GPM DPR and the level-2 products are still insufficient hampering a comprehensive understanding of its technical skills. Moreover, numerous studies have been focused to evaluating and exploring the level-3 gridded satellite- and reanalysis-based precipitation products, such as TMPA, GPM

IMERG and GSMaP, which combine the observations of a variety of sensors and instruments [30–35]. However, the similarities and differences between GPM DPR and TRMM PR, the level-2 radar only products, should be studied further and deeper, since these radars are used as calibration tools in the precipitation retrievals of the merged (or integrated) products [36]. Particularly, as yet, there is no study comparing the capability of the two radars to distinguish different types of hydrometeors and classify rain types (stratiform and convective). Different rain types are characterized by different precipitation growth mechanisms and different vertical distributions of the diabatic heating process. Thus, distinguishing precipitation types correctly is essential for better precipitation estimation [37–39]. Since GPM DPR and TRMM PR share almost the same fundamental ideas of retrieval algorithms, sensor configuration, as well as similar correction and validation systems [40,41], it is important to compare them directly to fully characterize their differences and similarities.

Therefore, the main objective of this study is to compare the performance of TRMM PR and GPM DPR at the global scale during their overlapping period, with special attention paid to their capability to classify rain types. We investigate not only the occurrence and the volume of different rain types, but also the distribution and the vertical structure of different rain types at a global scale. Results in this study are expected to contribute to a deeper understanding of the similarities and differences between the two radars, and the improvement of future versions of spaceborne radar precipitation retrieval algorithms. Researchers in many fields, including not only radar remote sensing development, but also meteorology and hydrology communities, will benefit from such research results when conducting their respective studies.

This paper is organized into four sections. Section 2 introduces the datasets used in this study and demonstrates the methodology. Section 3 presents the results and some discussion. Finally, Section 4 summarizes the main conclusions and provides a framework for future studies.

2. Data and Methodology

2.1. TRMM PR

In this study, we used the TRMM PR level 2 (L2) version 7 product 2A23 and 2A25. Main characteristics of TRMM PR are presented in Table 1. The TRMM satellite flies in a low-inclination (35°) and low-altitude (approximately 403 km after boost) orbit. TRMM PR scans 17° to either side of nadir at intervals of 0.35° with a vertical resolution of 250 m. PR has 49 footprints, each of which has a diameter around 5 km, meaning the horizontal resolution of PR is 5 km and the width of a swath is 247. The vertical resolution of TRMM PR is 250 m. According to the official files, the minimum detectable radar equivalent reflectivity factor, Z_e , and rainfall rate of TRMM PR are 18 dBZ and 0.7 mm/h, respectively, although studies have found that the actual detectability could be better [28].

Table 1. Brief description of GPM DPR and TRMM PR.

| Instrument | GPM DPR | | TRMM PR |
|--------------------------------------|--------------------------|----------------------|-------------------------------|
| | KaPR | KuPR | |
| Operating time | 27 February 2014—now | 27 February 2014—now | 27 November 1997—8 April 2015 |
| Altitude (km) | 407 | 407 | 403 ¹ |
| Inclination angle ($^\circ$) | 65 | 65 | 35 |
| Frequency (GHz) | 35.547 and 35.553 | 13.597 and 13.603 | 13.796 and 13.802 |
| Horizontal resolution at nadir (km) | 5 | 5 | 5 ¹ |
| (Swath width (km)) | (120) | (245) | (247) ¹ |
| Vertical resolution (m) | 250/500 | 250 | 250 |
| Minimal detectability (R, mm/h) | 0.2 | 0.5 | 0.7 |
| Minimal detectability (Z_e , dBz) | 12 (Ka_HS) 18 (Ka_MS) | 18 | 18 |
| Measurement Accuracy (dBz) | $<\pm 1$ | $<\pm 1$ | $<\pm 1$ |

¹ Numbers in the last column represent specifications after the TRMM boost in August 2001.

The TRMM PR L2 version 7 2A23 product detects the vertical profile of radar equivalent reflectivity, determines the heights of BB, as well as freezing level (the 0 °C isotherm), and classifies the precipitation into three categories: “stratiform”, “convective” and “other” [41]. Because the vertical profile of radar equivalent reflectivity factor, Z_e , the raindrop size distribution (DSD) and signal attenuation vary with rain type, it is critical to classify the rain type correctly in order to improve the accuracy of retrieval algorithms [42,43]. Numerous studies related to different rain types have been conducted [44,45], and it is widely understood that stratiform precipitation not only exhibits a layer of strong radar echo, named the “bright band”, but is homogeneous horizontally. In contrast, convective precipitation is characterized by horizontally localized cores of intense radar echoes and tall and thin columns with high reflectivity in vertical cross sections [46]. Two single-band algorithms, the vertical profile method (V-method) [47] and the horizontal pattern method (H-method) [48], have been established in TRMM PR to distinguish rain types, according to these differences [35,39,40]. Details can be found in [26,41,43,47]. The type “other” means there is only cloud (ice) and/or maybe the signal is simply noise [41].

The TRMM PR L2 version 7 2A25 product uses the output data from 1C21, 2A21 and 2A23 to produce an estimate of instantaneous three dimensional structure of attenuation-corrected radar equivalent reflectivity and rainfall at each angle beam [41,49]. For more details on the algorithm, please refer to [41,49]. Briefly speaking, the parameter used in our study is “near-surface rain rate”, which is estimated from the near surface reflectivity contingent on the rain types and corrected from non-uniform beam filling [49]. Near surface refers to the lowest range bin generally free from surface clutter [41,50]. From the nadir to the edge of the swath, the height of “near surface” varies from 500 m above the Ellipsoid to 2000 m [50].

2.2. GPM DPR

The Level 2 version 04A product of GPM DPR, 2ADPR, was used in this study. The GPM satellite was launched in February 2014 and did not reach its stabilized altitude for the nominal scan until April 2014.

The GPM Core Observatory operates in a non-sun-synchronous orbit, at an inclination to the equator of 65° and an altitude of 407 km. Since GPM DPR consists of the Ku-band and Ka-band precipitation radar, which are abbreviated as KuPR and KaPR, respectively, it has three scan patterns, one for KuPR and the other two for KaPR. Main characteristics of GPM DPR are presented in Table 1 as well. The scan pattern of KuPR is almost the same as that of TRMM PR. KaPR also has 49 footprints divided into two types of scans, the matched scan (Ka_MS) and the high-sensitivity scan (Ka_HS). In Ka_MS, whose swath width is 120 km, the beams are matched to the central 25 beams of KuPR. The other 24 beams of KaPR, forming the Ka_HS, are interlaced with the scan of KaPR’s matched beams. The nominal vertical range resolution of both radars is 250 m, sampled every 125 m [5]. In this study, we used the level 2 version 04A product 2ADPR. In the inner swath of the 2ADPR (the central 25 beams, referred to as 2ADPR_MS) we used both the KaPR and KuPR observations to make the attenuation correction, derive raindrop size distributions, classify the rain types and estimate precipitation. In the outer swath (corresponds to the 1–12 beams and 38–49 beams), only KuPR’s observation was available and used in the retrieval.

To make the best of the additional channel Ka-band, which can provide more information obtained from non-Rayleigh scattering effects at a higher frequency, a new dual-frequency algorithm, known as the measured dual-frequency ratio (DFRm) method, was proposed [40,51]. DFRm profile, obtained by taking the difference of the two frequency observations, holds rich information for melting layer detection and rain type classification. In the 2ADPR product, the results of the DFRm method, which are categorized into three types: “stratiform”, “convective” and “transition”, are merged with those of the Ku-only H-method, generating three major types: “stratiform”, “convective” and “other”, apart from the “missing” and “no data” categories. In the outer swath, V-method and H-method are combined to classify the precipitation types [51,52].

2.3. Methodology

The study area only focuses on the latitudes between 40°S to 40°N, although the area monitored by TRMM PR (37.5°S to 37.5°N) is slightly smaller than the area being studied. This study covers the time period from 1 April 2014 to 7 October 2014 and 12 February 2015 to 1 April 2015, since TRMM PR terminated collecting data on 8 April 2015. Figure 1 illustrates the spatial pattern of the overpasses of GPM DPR and TRMM PR orbits resampled to $2^\circ \times 2^\circ$. Both the two radars' scans are concentrated at the borders of the region studied, which is the latitude band from 35° to 37.5° and 35° to 40° for TRMM PR and GPM DPR respectively. It is clear that during the study period, TRMM PR passed the area more frequently and more uniformly due to its smaller inclination, compared with GPM DPR. Although the GPM developing team continues to upgrade the products and update some software applied to GPM DPR to improve the scan performance, we have ignored these changes in this study, as they are not significant [28].

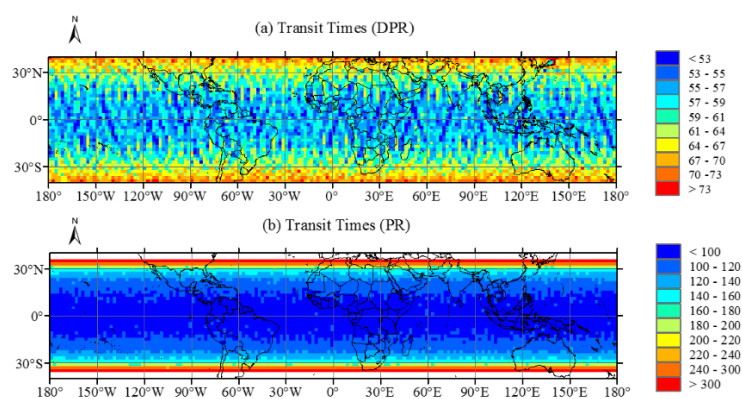


Figure 1. Numbers of transit times of: (a) the Global Precipitation Measurement mission dual frequency radar (GPM DPR); and (b) the Tropical Rainfall Measuring Mission Precipitation Radar (TRMM PR) within $2^\circ \times 2^\circ$ pixels. DPR is represented by its normal scan swath (DPR_NS).

To gain an intuitive knowledge of the detectability of TRMM PR and GPM DPR, we used all of the data available in the co-existing period of the two radars to conduct an overall comparison. The results applying the whole swath data are presented and discussed in Sections 3.1 and 3.2. Furthermore, since the TRMM PR scan pattern and GPM DPR normal scan pattern are very similar, we first selected the matchup pixels of all the DPR NS swath (referred to as DPR_NS) and TRMM PR swath within a time interval of 20 min and a space interval of two km same as those used in [29]. This matchup group is hereinafter referred to as Group 1. This relative large temporal difference is adopted to acquire adequate coincident events to support solid statistical analysis [29]. We also tried other time intervals ranging from 5 to 15 min. While the number of coincident events decreased remarkably as the time interval narrowed down (6,384,259 and 348,145 pairs for the time interval 20 and 5 min, respectively), little change was observed in the results. For example, the correlation coefficients of all the coincident events in Group 1 increased slightly, from 0.50 (with time interval of 20 min) to 0.66 (with time interval of 5 min). Only root mean square deviation (RMSD) and relative difference (RD) decreased sharply when the time interval of 5 min was adopted. More details are shown in Table 2.

Table 2. Metrics calculated for coincident events between GPM DPR and TRMM PR in Group 1.

| Time Interval (min) | Coincident Events | r | RMSD ¹ (mm/h) | MD ¹ (mm/h) | RD ¹ (%) | POD ¹ | FOH ¹ | FAR ¹ | CSI ¹ |
|---------------------|-------------------|------|--------------------------|------------------------|---------------------|------------------|------------------|------------------|------------------|
| 20 | 6,384,259 | 0.50 | 1.41 | 0.00 | 3.62 | 0.79 | 0.61 | 0.39 | 0.52 |
| 15 | 996,415 | 0.52 | 1.28 | 0.01 | 6.63 | 0.80 | 0.43 | 0.57 | 0.39 |
| 10 | 691,488 | 0.54 | 1.24 | 0.01 | 8.22 | 0.87 | 0.40 | 0.59 | 0.54 |
| 5 | 348,145 | 0.66 | 0.49 | 0.00 | 0.23 | 0.89 | 0.35 | 0.65 | 0.49 |

¹ The metrics are calculated with TRMM PR serving as the benchmark.

In the overlapping period, 6,384,259 pairs of matchup data were acquired in Group 1. Because 2ADPR contains results from both dual-frequency and single frequency retrieval algorithms, it is necessary to take this into consideration when processing the matchup procedure. For TRMM PR, previous studies have pointed out that because of angle dependency in the outer swath, the near-nadir (NN) statistics are assumed to be of the highest quality in terms of observation limitation [53]. Kubota et al. [54] found that the sidelobe clutter in KuPR in DPR is stronger than that in TRMM PR, and thus, it cannot be ignored. Therefore, we then selected the matchup pixels of DPR MS swath and TRMM PR inner swath (the central 25 beams) within the same time and space interval as Group 1. This new group is hereinafter referred to as Group 2, containing 1,237,875 pairs of pixels. To get a deeper insight into the difference between Group 1 and 2, pixel pairs of Group 2 are excluded from Group 1. This new group is hereinafter referred to as Group 3. For each coincident event of three matchup groups, we not only matched and compared the estimated precipitation and the rain type classification, but also the height of freezing level and BB to gain a deeper understanding of the vertical structure of precipitation, especially for stratiform precipitation. The results are presented in detail in Section 3.3. Although there exists some latitudinal sampling bias associated with the orbital characteristic of the TRMM satellite and the GPM satellite, the effect can be ignored because the ratio of the observed pixels at each latitude, counting to that at the equator, increases slightly within the domain studied in this paper [28].

3. Results

3.1. Global Distribution of Different Precipitation Types

Figure 2 shows the global distribution of the average precipitation estimates of different rain types resampled directly from the level 2 products of GPM DPR and TRMM PR at a spatial resolution of $2^\circ \times 2^\circ$. Concerning the spatial pattern of all types of precipitation, the observations of TRMM PR and GPM DPR agree with each other very well in tropical and subtropical regions. The spatial patterns shown in Figure 2 are similar to those shown in [45], which were based on eight-year observations of TRMM PR. The intertropical convergence zone (ITCZ), the Indian Ocean and South Pacific convergence zone (SPCZ) have the greatest precipitation, while the regions off the west coast of South America and South Africa, the Arabian Peninsula and North Africa have the lowest precipitation. Previous studies have shown that TRMM PR agrees fairly well with the GPCC gridded gauge analysis and rain gauge measurements in capturing rainfall in the Sahara during a 15-year period [55]. However, it is clear that TRMM PR gives a higher estimation of precipitation globally than GPM DPR. This phenomenon may result from the fact that TRMM PR passes the studied region more frequently and is more likely to capture precipitation events. When comparing TRMM PR and GPM DPR in Japan, a similar phenomenon was observed [56]. While TRMM PR passes the southern part of mainland Japan at least once a day, GPM DPR passes Japan once every four days on average. Due to the lower visiting frequency in tropical and subtropical regions, GPM DPR tends to miss some precipitation events [56].

Convective and stratiform precipitation have different statistical behavior over land and ocean. Specifically, convective precipitation attains higher rain rates over land while a large amount of stratiform precipitation occurs over the ocean [44]. It is generally believed that stratiform precipitation exists mostly in mid-latitude regions, and in baroclinic cyclones and fronts [46]. However, both TRMM PR and GPM DPR indicate that stratiform precipitation is also widely distributed in tropical regions, where convective precipitation dominates. This result is supported by the research of Robert and Houze [46], which shows that stratiform precipitation can be found within a region where the convection is weak and less vigorous. According to [44], stratiform precipitation is rare in regions off the east coast of South America and Southern Africa, contributing to less than 20% of the total precipitation. Together with the relatively low revisiting frequency, it is understandable that both of the two spaceborne radars insufficiently detected stratiform precipitation in these regions, although TRMM

PR captured slightly more stratiform precipitation than GPM DPR. According to [57,58], shallow isolated rain makes up a large portion of the total rainfall in the southern Indian and Pacific oceans.

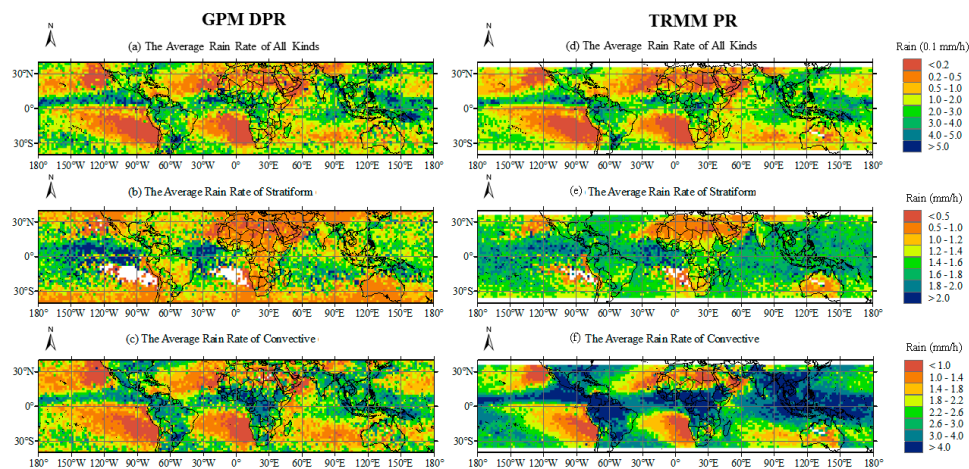


Figure 2. Global distribution of precipitation of: (a,d) all kinds; (b,e) stratiform; and (c,f) convective. Panels (a–c) are for GPM DPR; and Panels (d–f) are for TRMM PR. All data are resampled to a spatial resolution of $2^\circ \times 2^\circ$ and the average rain rates are obtained by calculating the average based on all the precipitation events captured by spaceborne radars.

Note that the average rainfall rate of convective or stratiform precipitation is higher than that of total precipitation. Moreover, the average rainfall rates of some grid cells in Figure 2a,d are lower than 0.2 mm/h, which is even lower than the official minimum detectable thresholds of the two radars. These phenomena are partly due to the fact that from the result in our study presented later in Section 3.3.1 and Hamada et al. [28], the official definition of minimum detectable rainfall rates may be too conservative for both radars [27]. Another reason is the computational method we adopted. When calculating the average rainfall during the whole study period, we first selected all the pixels that fell into the same grid cell and were of the same rain type in one scan granule. Then, we calculated the average rainfall rate of these pixels and regarded it as the rainfall rate of one precipitation event. Finally, we calculated the arithmetic mean as the average rainfall rate, using all precipitation events during the whole study period. It is noted that one precipitation event may consist of pixels categorized as “stratiform”, “convective” and “other” types at the same time. As Peng et al. [59] stated, “other” precipitation is often characterized by cumulonimbus anvils, whose rain rates are generally very low. According to [40,41,51], pixels classified as “other” are unclear and sometimes may not even contain precipitation. In summary, the precipitation rates of other-type are usually lower than those of “stratiform” or “convective” precipitation. It is reasonable that the average precipitation rate of stratiform and convective precipitation is higher than that of total precipitation. Since convective precipitation is usually the heaviest, with precipitation rates higher than those of stratiform precipitation, the average rate of convective precipitation may naturally exceed that of both stratiform and total precipitation.

Figures 3 and 4 show the global distribution for stratiform and convective precipitation as a fraction of the total precipitation volume captured by GPM DPR and TRMM PR, respectively. Although stratiform precipitation is distributed both in the tropical regions and the middle latitudes, it accounts for the majority of precipitation in the latter. The results in Figures 3 and 4 are comparable with [44], which found that contributions due to convective precipitation over the Atlantic, Indian Ocean and the western tropical area of the South Pacific Ocean generally exceed 50%. Within the Pacific Ocean’s ITCZ, convective precipitation generally exceeds 50% [44].

TRMM PR and GPM DPR exhibit very similar spatial distributions in terms of convective and stratiform precipitation fractions, with the difference between the two radars ranging from -10% to 10% . This is reasonable considering that TRMM PR and GPM DPR adopt similar rain type classification

methods. The most significant differences occurred in North Africa, the Arabian Peninsula, Southern Africa and the regions off the west coast of North America and Australia (results not shown). GPM DPR distinguished more stratiform precipitation in the first three regions, and the difference between the fractions of the two radars was as high as approximately 40%. However, in the latter two regions, GPM DPR classified 35–40% more precipitation as convective, compared with TRMM PR.

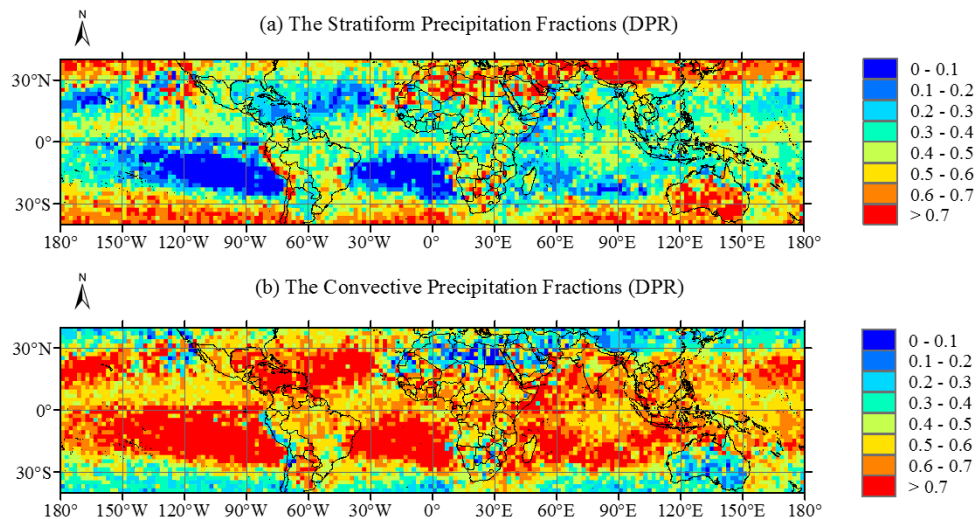


Figure 3. Global distribution of the fractions for: (a) stratiform; and (b) convective precipitation in the total precipitation volume captured by GPM DPR. All data are resampled to a spatial resolution of $2^\circ \times 2^\circ$ and the fraction is calculated as the ratio between the accumulated stratiform/convective precipitation volume and the total precipitation volume.

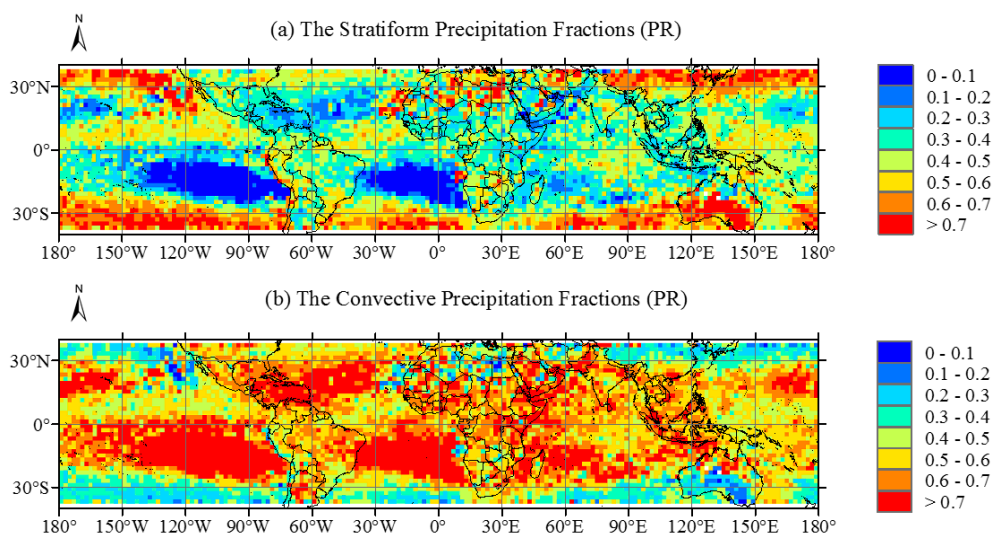


Figure 4. Global distribution of the fractions for: (a) stratiform; and (b) convective precipitation in the total precipitation volume captured by TRMM PR. All data are resampled to a spatial resolution of $2^\circ \times 2^\circ$ and the fraction is calculated as the ratio between the accumulated stratiform/convective precipitation volume and the total precipitation volume.

3.2. Global Distribution of Freezing Level and BB Heights

BB has a significant influence on the classification quality in both the V-method applied in the TRMM PR retrieval and the DFRm applied in the GPM DPR retrieval. We used 2A23 and 2ADPR datasets to draw maps of the distribution of average BB height and the average height of freezing level,

which is closely related to the BB (Figures 5 and 6) because BB is detected in a search window with the freezing level at its center [26,40]. In general, GPM DPR gives slightly higher estimates of the freezing level height in tropical regions, and lower estimates in the middle latitudes compared with TRMM PR. The difference between the freezing level estimates given by the two radars is within ± 100 m at low latitudes and below -100 m in the Southern Hemisphere at middle latitude.

As for the distribution of the average BB height, GPM DPR and TRMM PR exhibited notable differences. GPM DPR presents a lower estimate of the BB height at low latitudes, especially over the ocean, except in the Andes in Peru and Bolivia, where GPM DPR's estimate is 1 km higher than that of TRMM PR. It is noted that in these areas, the estimate of freezing level also exhibits some discrepancy, as GPM DPR presented a relatively lower estimate of freezing level. In North Africa, the Middle East and the Tibetan Plateau, the average BB height of GPM DPR was about 1 km higher than that of TRMM PR. As shown in Figure 2, both the two radars failed to detect the BB where they did not find stratiform precipitation over the ocean, but the blank region is larger compared with that in Figure 2. This is because, although BB can indicate the existence of stratiform precipitation, precipitation can be classified as stratiform even without BB in H-method. The H-method first detects convective precipitation first and then categorizes rain as stratiform when the rain type is not convective and the rain echo exists [43]. When using these datasets in future studies, researchers should bear these differences in mind.

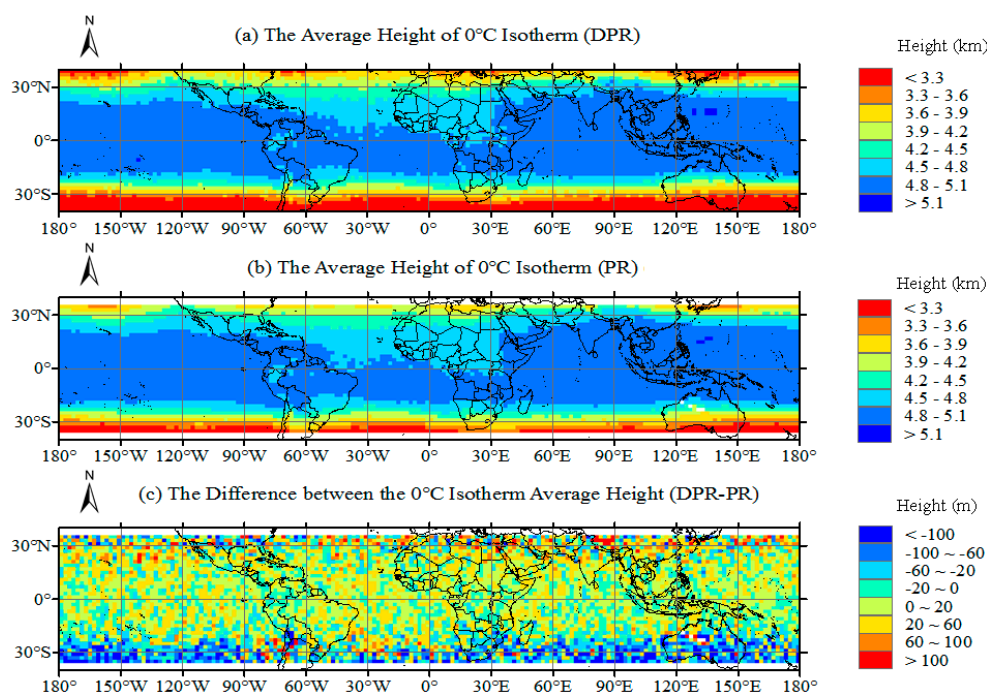


Figure 5. The distribution of the average height of freezing level captured by: (a) GPM DPR; and (b) TRMM PR. The difference between the observations of the freezing level height is shown in (c), calculated by GPM DPR's observation minus TRMM PR's. All data are resampled to a spatial resolution of $2^\circ \times 2^\circ$.

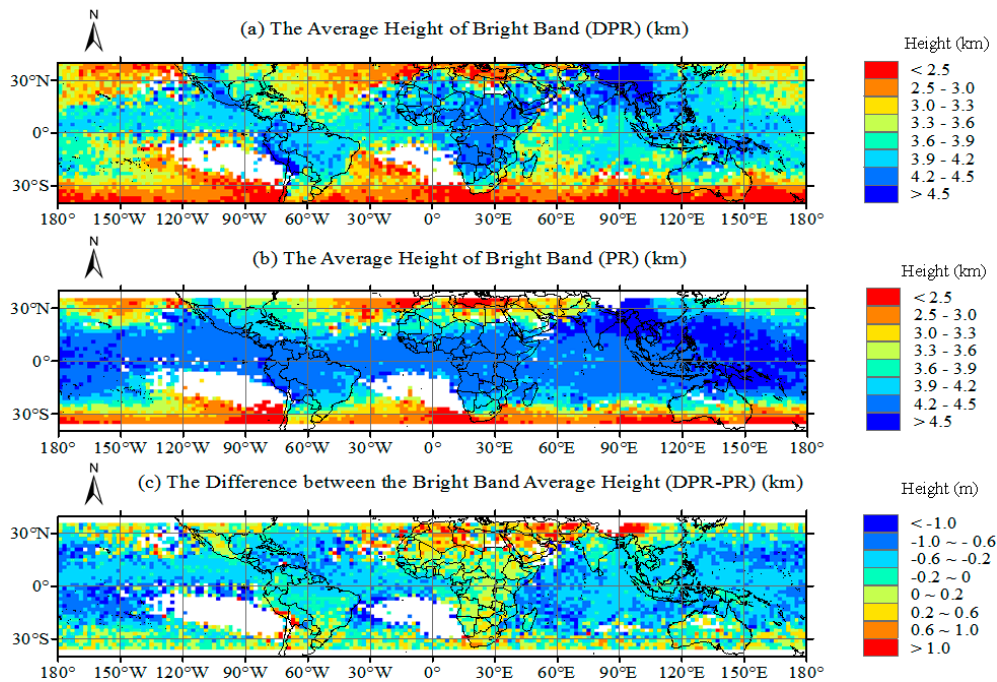


Figure 6. The distribution of the average height of bright band captured by: (a) GPM DPR; and (b) TRMM PR. The difference between the observations of the bright band height is shown in (c), calculated by GPM DPR's observation minus TRMM PR's. All data are resampled to a spatial resolution of $2^\circ \times 2^\circ$.

3.3. Comparison of Precipitation Estimates Based on Matchup Events

3.3.1. Comparison of Overall Precipitation

To obtain a deeper understanding of the similarities and differences between GPM DPR and TRMM PR, the two radars were compared directly based on their global matchup events. Metrics, such as the correlation coefficient (r), root mean square deviation (RMSD), mean difference (MD), and relative difference (RD), were calculated for Groups 1–3, with TRMM PR serving as the benchmark. Furthermore, we also calculated the probability of detection (POD), the frequency of hit (FOH), the false alarm ratio (FAR) and the critical success index (CSI) for the three groups. Generally, GPM DPR corresponded well with TRMM PR in Group 1 and 3, but, in Group 2, the results are a little worse (Table 3). Special attention should be paid to RD, as it decreases from 3.62% (in Group 1) to -4.46% (in Group 2). In Group 3, the RD and the r are 5.00% and 0.53 respectively. The POD and CSI, which are 0.80 and 0.53, respectively, are both highest among the three groups. This suggests that the dual-frequency retrieval algorithm gives a lower estimate of precipitation rates. The higher consistency between TRMM PR and GPM DPR in Group 1 is attributed to the fact that some pixels of GPM DPR apply single frequency (Ku-band) retrieval algorithm.

Table 3. Metrics calculated between GPM DPR and TRMM PR.

| Matchup Groups | r | RMSD (mm/h) | MD (mm/h) | RD (%) | POD | FOH | FAR | CSI |
|----------------|------|-------------|-----------|---------|------|------|------|------|
| One | 0.50 | 1.41 | 0.00 | 3.62 | 0.79 | 0.61 | 0.39 | 0.52 |
| Two | 0.38 | 1.42 | 0.00 | -4.46 | 0.76 | 0.59 | 0.41 | 0.49 |
| Three | 0.53 | 1.19 | 0.00 | 5.00 | 0.80 | 0.61 | 0.39 | 0.53 |

Figure 7 illustrates the detection of overall precipitation of the two radars in Groups 1–3. Although Group 2 only contains the coincident events in the inner swath, the results are very similar to those in Group 1 and 3. Figure 7 shows that both TRMM PR and GPM DPR have the ability to detect some extremely light precipitation events, with intensities smaller than their official minimum detectable

thresholds, i.e., 0.2 and 0.7 mm/h, respectively. The official definition of minimum detectable rainfall rates may be too conservative for both radars [28].

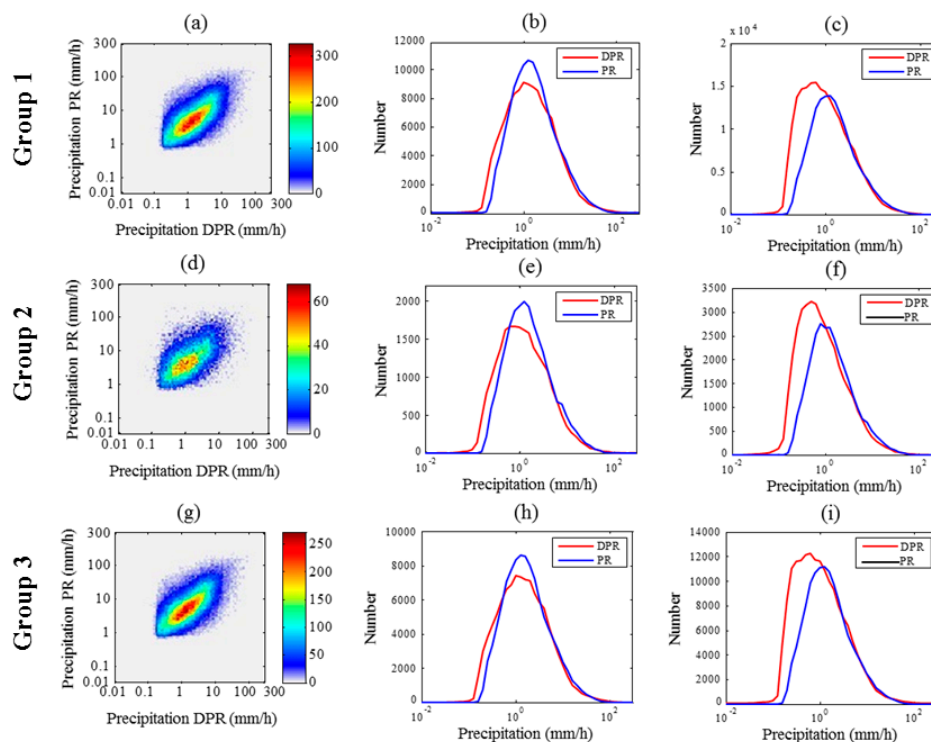


Figure 7. (a,d,g) Scatter plots between TRMM PR and GPM DPR based on global coincident precipitation events. The color represents event numbers for each grid corresponding to different precipitation intensities of two radars. (b,e,h) Precipitation frequency distributions of GPM DPR and TRMM PR based on coincident events when both radars generate positive estimates. (c,f,i) Precipitation frequency distributions of GPM DPR and TRMM PR based on coincident event when at least one radar generates positive estimates. The figures correspond to Groups 1–3 from top to bottom rows, respectively.

GPM DPR significantly improved the detection of precipitation events, especially for light precipitation, as shown in Figure 7c,f,i. In the three groups, the occurrences of all kinds of precipitation and light precipitation (rain rates < 1 mm/h) detected by DPR were ~1.7 and ~2.53 times greater than that of PR.

The TRMM satellite orbit was raised from 350 km to 402.5 km, resulting in a sensitivity degradation of 1.2 dB, while the receiver DPR noise of TRMM PR remained unchanged [60]. Therefore, TRMM PR is more likely to miss weak and light precipitation since the rain echo is obscured. Moreover, TRMM PR's footprint size as well as the clutter-free bottom increased after the boost, an indication that shallow rain systems, which mainly consist of light precipitation are more often missed by TRMM PR [60,61]. Liang et al. [62] and Nakazawa et al. [63] all found that after the boost the amount of weak convective precipitation decreased. In the meantime, it seems that this is not a problem for GPM DPR, because it shares the same footprint size and orbit altitude with TRMM PR. Some researchers have pointed out that the sensitivity of both KaPR and KuPR in GPM DPR is higher than that of TRMM PR [64,65]. This is achieved by increasing the transmitting power of KuPR and using variable pulse repetition frequency, which can optimize the sampling of precipitation echoes [56].

For precipitation larger than 3 mm/h, TRMM PR and GPM DPR agree with each other quite well, with their frequency distribution curves almost overlapping. However, Figure 7b,e,h show that, when GPM DPR and TRMM PR both observe precipitation at one coincident event, TRMM PR tends

to slightly overestimate precipitation, with rain rates ranging between 0.6 and 3 mm/h greater than GPM DPR.

Since the performance of the two radars varies with the magnitude of rain rates, we classified the precipitation events according to their rainfall rates and calculated the accumulated precipitation based on the coincident events in Group 2 and 3 (Figure 8). Results suggest that, for both light and extreme precipitation, TRMM PR misses a large percentage of precipitation events that are caught by GPM DPR. A huge number of light precipitation events (rain rate < 1 mm/h) caught by GPM DPR were missed by TRMM PR. However, for precipitation with rain rates ranging between 10 and 50 mm/h, the two radars performed similarly. Since the spaceborne radars produce instantaneous estimates of rain rate and the matchup interval of this study was set to 20 min, the two radars may scan from different angles and receive different profiles of radar reflectivity for the same coincident precipitation. Similar to matching spaceborne radar and ground-based radars, matching PR and GPM DPR encounters problems introduced by the measurement of return signals from different volumes of the precipitation medium, and changes in the satellite altitude and velocity, due to orbit eccentricity [66].

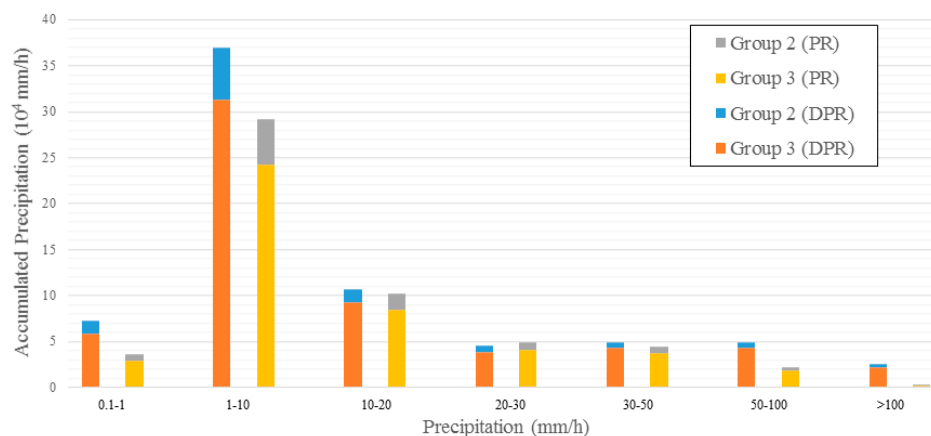


Figure 8. Histograms of accumulated precipitation based on global coincident events between DPR and PR in Group 2 and 3.

3.3.2. Comparison of Rain Types

Table 4 shows the rain type classification results for TRMM PR and GPM DPR for matchup Groups 1 and 2. Generally speaking, the difference in the statistical results between Groups 1 and 2 is small. We also checked up on the rain type classification results for matchup Group 3 mentioned in the above section. The results (not shown) are almost the same with those for Group 1. GPM DPR has no missing data while TRMM PR has 6.06% and 5.53% of the total matchup pixels without data in Groups 1 and 2, respectively. This indicates that GPM DPR has a better detectability of precipitation. Previous studies, which used ground radars in parts of the USA and Australia and over the Pacific Ocean as the criteria, also suggest that TRMM PR tends to under-detect rainfall occurrences on account of its low sensitivity, especially for stratiform precipitation [18,19,67]. In Group 1, the percentage of “other” for TRMM (10.14%) PR is almost 20 times larger than that of GPM DPR (0.51%), and the percentages of “no rain” for TRMM PR and GPM DPR are 80.85% and 94.94%, respectively. The results of classification as “no rain” and “other” are similar in both groups for GPM DPR, but TRMM PR classifies even more events as “other” in Group 2 than in Group 1. It is reasonable to infer that TRMM PR tends to mistake “no rain” events as “other” more often than GPM DPR. According to the classification method of TRMM PR, the rain type is determined at the pixel scale and remains the same along the radar beam. It is difficult for TRMM PR to distinguish the rain type in case the precipitation echo only exists at the altitude higher than the freezing level [40]. Hence, for TRMM PR, the rain type “other” includes cases where radar echoes are actually reflecting clouds or just noise, which should be categorized as “no rain”. This problem is ameliorated significantly in GPM DPR. Awaka et al. [51] point out that by

improving the sidelobe clutter rejection algorithm in the VER module in DPR, the count of rain type “other” is significantly reduced.

Table 4. The rain type classification results for TRMM PR and GPM DPR based on all the coincident events.

| Instruments | Matchup Groups | Total | Stratiform | Convective | Other | No Rain | Missing |
|-------------|----------------|-----------|------------------|------------------|-------------------|---------------------|------------------|
| PR | Group 1 | 6,384,259 | 133,199 2.09% | 54,671 0.86% | 647,592 10.14% | 5,161,757 80.85% | 387,040 6.06% |
| | Group 2 | 1,237,875 | 28,515 2.30% | 13,104 1.06% | 168,146 13.58% | 959,708 77.53% | 68,402 5.53% |
| DPR | Group 1 | 6,384,259 | 188,988 2.96% | 101,698 1.59% | 32,571 0.51% | 6,061,002 94.94% | 0 0.00% |
| | Group 2 | 1,237,875 | 32,920 2.66% | 19,545 1.58% | 6189 0.50% | 1,179,221 95.26% | 0 0.00% |

GPM DPR can distinguish between rain types more clearly, because in Table 4 its ratios of the “stratiform” and “convective” precipitation are higher compared with TRMM PR. This is due to multiple factors. First, and most importantly, the detectability of GPM DPR has been improved significantly, thus making it possible for GPM DPR to detect lighter radar echoes and receive more precipitation information, which are helpful for rain type classification. Second, the rain type classification methods for examining the vertical profiles of radar equivalent reflectivity adopted in TRMM PR and GPM DPR are quite different. The former uses single band algorithm V-method, detecting the BB near the freezing level to determine whether the rain type is stratiform. However, the latter one uses the DFRm method, which combines the vertical profiles of radar equivalent reflectivity observed by both the KuPR and KaPR by calculating their difference and defining several indices. Since the DFRm is controlled by the non-Rayleigh backscattering effect and the path integrated attenuation (PIA) differs between the two bands, the vertical profiles of DFRm for stratiform and convective precipitation differ significantly from each other, as a result of their distinctive microphysical mechanisms and particle distributions [51]. The DFRm is able to handle more additional information, improving the precision of light precipitation. Awaka et al. [52] found that by applying DFRm, the BB count is increased in inner swath, which can help improve type classification. Moreover, a parallel procedure, which is executed under multiple assumptions, is conducted in GPM DPR’s dual-frequency algorithm, if the precipitation types cannot be determined with confidence in CSF module [40]. This is helpful for determining the precipitation types afterwards. All of these factors contribute to the improvement in the precipitation type classification of GPM DPR.

Figure 9 shows the frequency distributions for stratiform and convective precipitation based on coincident events (including events where just one radar observes precipitation) in Groups 1 and 2. GPM DPR detects more light stratiform and convective precipitation than TRMM PR, which is consistent with the result for all precipitation types shown in Figure 7c. Nevertheless, as shown in Figure 7b, TRMM PR detects more moderate and heavy precipitation of both the two types, especially for convective precipitation. Because convective precipitation is usually more intense than stratiform precipitation, it is reasonable that in Figure 9b,d the curves of TRMM PR exceed those of GPM DPR in zones of moderate and heavy rain rates. This is more significant in Group 2. Several studies have discovered that as a result of low BB height, large path-integrated attenuation (PIA) and strong correction, PR is likely to overestimate the convective rain rate in the Korean Peninsula and some other regions compared with ground radars [68,69]. Chen et al. [70] found that due to incorrect rain type classification, overcorrection of radar signals, poor performance of the Surface Reference Technique (SRT) module, ground clutter and geometric effects, TRMM PR overestimates the frequency of moderate rain rates. GPM DPR was found to underestimate precipitation rates for rates smaller than 10 mm/h and overestimate for rates above 10 mm/h by using at-launch code and synthetic data based on the TRMM PR data [71].

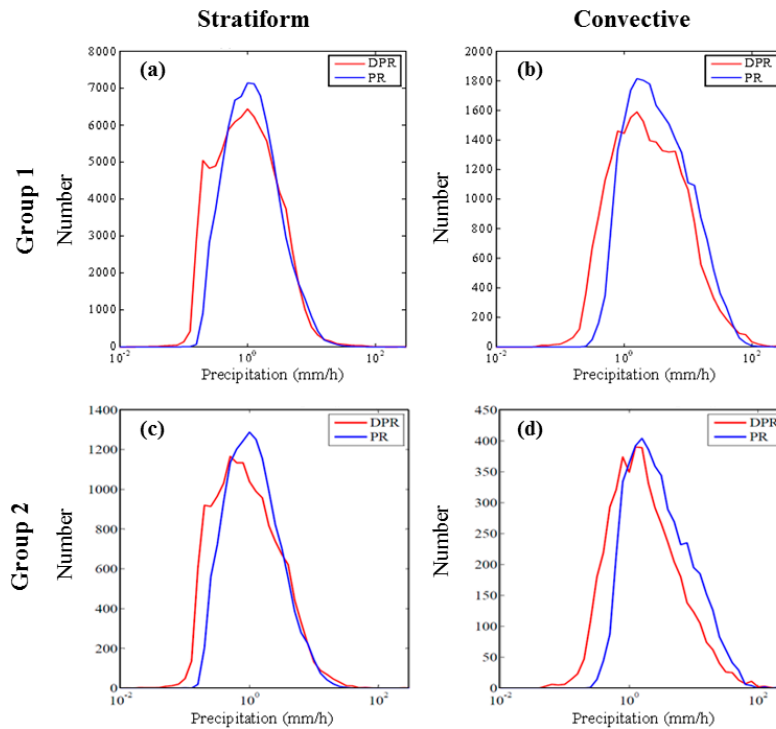


Figure 9. Frequency distributions for: (a,c) stratiform; and (b,d) convective precipitation estimates based on the coincident events in Group 1 and 2. The coordinates in x-axis is exponential, ranging from 0.01 to 300 mm/h and divided into 50 bins.

Tables 5 and 6 summarize the ratios of different precipitation types for TRMM PR and GPM DPR based on nonzero coincident events in Groups 1 and 2, respectively. As previously mentioned, DFRm enables GPM DPR to obtain more information about rain types. Nevertheless, no significant difference was discovered between the two groups. Results from the Ku-only rain type classification method were quite close to those from DFRm method, a finding supported by the conclusion in [52,72]. By applying one-month data of GPM 2ADPR, the results given by DFRm and Ku-only V-method were found to be highly consistent. Results in [52] discovered that only 14% of the inner swath data used the DFRm method. This also confirms that the decisions made by Ku-only method and DFRm method are reliable.

Table 5. The number of matchup pixels in Group 1 (all NS swath) between TRMM PR and GPM DPR, categorized according to precipitation types determined by two datasets. The numbers in parentheses are frequencies relative to the total for each TRMM PR precipitation type (%).

| | | DPR (All NS Swath, Group 1) | | |
|--------------------------------------|------------|-----------------------------|------------|--------|
| | | Stratiform | Convective | Other |
| PR (All NS swath, Group 1) | Stratiform | 82.89% | 16.07% | 1.04% |
| | Convective | 28.45% | 71.02% | 0.53% |
| | Other | 37.88% | 24.62% | 37.50% |

Table 6. The number of matchup pixels in Group 2 (the inner 25 beams) between TRMM PR and GPM DPR, categorized according to precipitation types determined by two datasets. The numbers in parentheses are frequencies relative to the total for each TRMM PR precipitation type (%).

| | | DPR (Inner 25 Beams, Group 2) | | |
|--|------------|-------------------------------|------------|--------|
| | | Stratiform | Convective | Other |
| PR (Inner 25 beams, Group 2) | Stratiform | 82.83% | 16.02% | 1.15% |
| | Convective | 24.91% | 74.17% | 0.92% |
| | Other | 45.20% | 28.76% | 26.02% |

Most of the stratiform precipitation categorized by the TRMM PR algorithm corresponded to that determined by GPM DPR. Around 16.07% and 16.02% of the stratiform precipitation of TRMM PR was categorized as convective precipitation by GPM DPR in Groups 1 and 2, respectively. Schumacher and Houze [44] found that because of TRMM PR's low horizontal resolution and attenuation, some convective echoes may be identified as stratiform. Around 71.02% of the convective precipitation determined by TRMM PR was also categorized as "convective" by GPM DPR, while 28.45% of the convective precipitation in TRMM PR was classified as "stratiform" by GPM DPR. In Group 2, the two indexes were 74.17% and 24.91%. By setting the time and space offsets to 3 min and 2 km, Hamada and Takayabu [28] obtained 14 matchup observations between GPM DPR and TRMM PR, which were used to compare their precipitation type classification results. The match percentages between the two radars for stratiform and convective precipitation are 85.37% and 38.32%, respectively [28]. Because they used precedent DPR Level 2 version 03B product, which is different from the data used in this study, plus the fact that the sample size of their study is quite small, it is reasonable that the results presented by our study are a little different from their results [28]. Nevertheless, the classification of rain type as "other" differs significantly between the two radars. For precipitation classified as "other" by TRMM PR, 37.88%, 24.62% and 37.50% of the observations were classified as "stratiform", "convective" and "other", respectively, by GPM DPR. This result is acceptable because the rain type "other" in both products contains a variety of precipitation, even including some non-precipitation cases [40]. Further studies are needed to adjust the algorithms to improve the classification quality.

3.3.3. Comparison of the Vertical Structure of Precipitation

The difference between Groups 1 and 2 in rain type classification is not significant according to the results described above. Awaka et al. [52] also pointed out that only 14% of the inner swath data used the DFRm method. With regard to the vertical structure of precipitation, we mainly focus on the freezing level height and BB height, which are closely related to the classification of stratiform precipitation. Considering that the sample size of Group 1 is 5.15 times greater than that of Group 2, we only used the coincident events in Group 1 for further study related to the vertical structure of precipitation to reduce uncertainty.

Figure 10 shows the scatter maps and the frequency distributions of the freezing level heights and BB heights based on the global matchup precipitation events between TRMM PR and GPM DPR. The heights of both freezing level and the BB detected by TRMM PR and GPM DPR correspond with each other very well, with correlation coefficients of freezing level and BB heights equal to 0.997 and 0.947, respectively. Furthermore, the frequency distribution curves of the two radars' observations almost overlap. However, there is a clear discrepancy between freezing level heights of TRMM PR and GPM DPR, which leads to the strange scatter distribution shown in Figure 10a. For example, TRMM PR produced some freezing level height estimates, shown in the red boxes, around 3 km, while for GPM DPR were below 2 km. The red boxes consist of 2779 pixel pairs and the sample size is quite small compared to the total number of pixel pairs (4,651,138). Through careful data examination, we found that this discrepancy appears mainly over the ocean and in mountainous regions, such as the central Andes Mountains, Zagros Mountains in Northern Iran, Hindu Kushi Mountain in Afghanistan, etc. For all the pixels in red boxes, no bright band was observed. According to [40,41], the freezing level heights in GPM DPR and TRMM PR are both computed using ancillary data (Global Analysis product, GANAL, produced by Japan Meteorological Agency) through linear temporal and spatial interpolation. Therefore, high consistency between the two radars' estimates of freezing level height seems to be apparent. However, the resolution of GANAL is different for TRMM PR and GPM DPR. It is $1.25^\circ \times 1.25^\circ$ for TRMM PR and $0.5^\circ \times 0.5^\circ$ for GPM DPR. The difference between the ancillary data may contribute to the discrepancy because uncertainties can be introduced in the interpolation process.

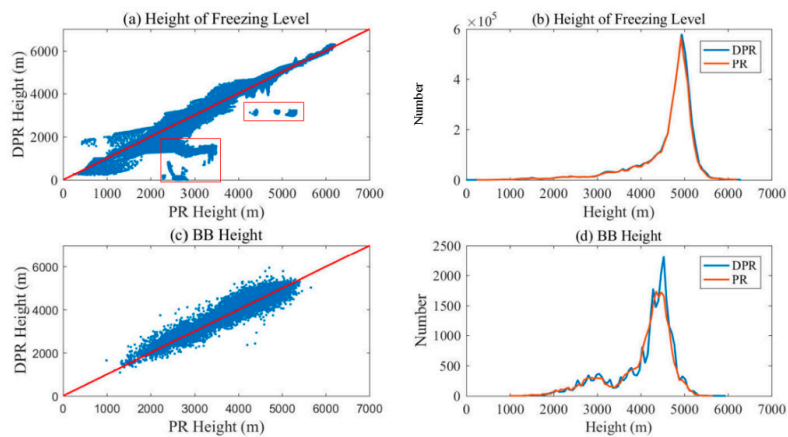


Figure 10. (a) Scatter plot; and (b) frequency distributions for freezing height level; and (c) scatter plot; and (d) frequency distributions for BB height. All figures are based on the coincident events of GPM DPR and TRMM PR. The red lines in (a,c) indicate where y equals x .

After eliminating these pixels, the r was improved from 0.997 to 0.998. By calculating the difference of the freezing level height between the two radars and analyzing its global distribution, we found that GPM DPR tends to underestimate the freezing level height by approximately 100 to 400 m. During the studied time period, the average height of freezing level globally was 4378 m for GPM DPR and 4367 m for TRMM PR. The estimation of BB heights was closely related to the freezing level heights, the former generally appearing about 0.5 km below the latter, based on empirical evidence [40,73]. Therefore, the BB height derived from GPM DPR observations is slightly lower than that from TRMM PR.

Special attention should be paid to the phenomenon that appears in the frequency distribution curves of the BB heights, in which both radars' observations have two peaks. One was around 4.5 km and the other near 3 km. However, this is inconsistent with the tendency shown in the frequency distribution curves of the freezing level, which are unimodal curves with the same peak value of 5 km. The pixels with BB heights around 3 km given by GPM DPR, distributed randomly over the ocean, making it difficult to find a clear regularity. Pixels with BB height around 3 km given by TRMM PR, were predominately located near 37°N/S over the ocean. At the pixels where GPM DPR gives BB heights around 3 km over the ocean, the estimate of the freezing level heights given by two radars were highly consistent. However, TRMM PR failed to detect BB at these pixels. The difference between freezing level height and BB height for most of these pixels was within 700 m. Since the sample size of freezing level height is much larger than that of BB height, the curves of freezing level are unimodal. Further studies are needed to investigate the actual causes for the abnormally low freezing level height and BB heights.

However, because the structures of convection vary with different updraft characteristics, the microphysical composition and horizontal dimensions of the hydrometeors [74], convective precipitation is too complicated to make a direct comparison as we have done for stratiform precipitation. Greater efforts should be extended into the study of precipitation mechanisms and the exploration of the interactions between precipitation particles and radar's echo to obtain accurate Z-R relationships.

3.3.4. Comparison of Precipitation on Different Surface Types

When using ground-based instruments, such as the rain gauges and ground-based radars, to observe precipitation events, researchers often have difficulty obtaining sufficient data of good quality [29]. This is particularly true over remote mountainous regions and ocean due to the sparse distribution and uneven coverage of these observation instruments [29]. TRMM PR and GPM DPR have played an important role in providing precipitation estimates over the global oceans and remote regions. Moreover, surface conditions can affect the radar signals. For example, the surface backscattering cross

section increases with surface soil moisture over land [14]. Hence, it is important to study the features of precipitation estimates produced by the two radars on different surface types.

In the GPM 2ADPR product, a parameter, “landSurfaceType”, produces the surface classification consisting of four categories: land, ocean, coast and inland water. Using this as an indicator of surface type, we divided all the coincident events in Groups 1–3 into these four categories, respectively. The results show that the coincident events occurring over inland water and with nonzero precipitation rates observed by at least one radar are very limited, with only 220, 5 and 215 pixel pairs in Groups 1–3 respectively. Because the areas of inland water, such as lakes and reservoirs, are usually small, considering the space interval of the matchup pixel pairs is 2 km, the coincident events we selected here may not be sufficiently representative. Therefore, we only analyzed the coincident precipitation events occurring over the other three surface types.

The number of precipitation events captured by TRMM PR is smaller than that captured by GPM DPR on all surface types, mainly due to the differences in light precipitation. Figure 11 shows the frequency distributions based on the coincident precipitation events over different surface types. GPM DPR captured more precipitation events, with rainfall rates below 1 mm/h, than TRMM PR. However, when the rainfall rate exceeded 1 mm/h, TRMM PR developed a slight trend in catching more precipitation than GPM DPR, particularly over coast and land. However, in Figure 11b, which illustrates the situation over the ocean, the performance of the two radars is quite close, confirming that the transition from TRMM to GPM is smooth. It is noted that the curves in Figure 11d–f are less smooth, which mainly results from the fact that Group 1 has a larger sample size. Similar to the results shown in Figure 7, the difference among Groups 1–3 is small, as the trends of curves are almost the same, regardless of surface types. The differences in retrieving precipitation in the inner and outer swath of DPR, which is discovered in Table 3, cannot manifest themselves in this part of our study, due to the fact that our classification is rather rough and we mainly focus on global scale. Recent studies suggest that relatively higher uncertainties exist in satellite-based precipitation estimates over coastlines and surface water bodies [32]. Considering the discrepancy in observations of freezing level height and BB height over complex terrains, such as mountainous regions like the Rockies and the Andes, where the uncertainties in rain rate estimates are evident [32], further studies should focus on these regions to explore the spaceborne radars’ performance more in-depth. Some ancillary data such as atmospheric data and ground-based observations are also required.

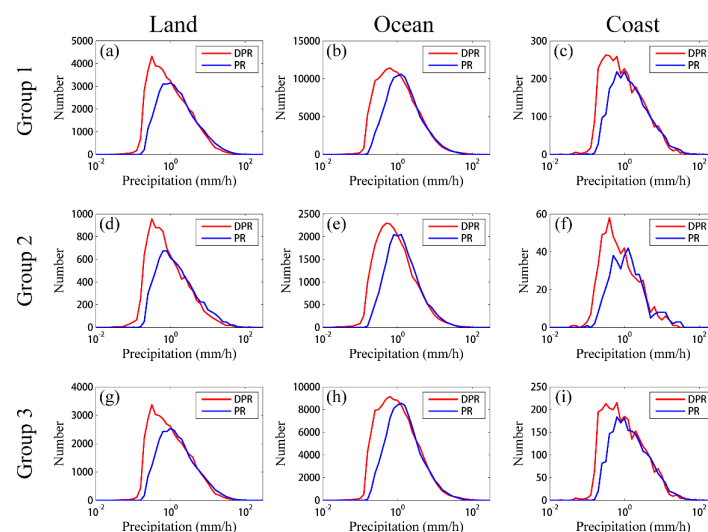


Figure 11. The frequency distributions for precipitation occurring over: (a,d,g) land; (b,e,h) ocean; and (c,f,i) coast, based on the coincident events. Panels (a–c) are based on Group 1; Panels (d–f) are based on Group 2; Panels (g–i) are based on Group 3. The coordinates in x -axis is exponential, ranging from 0.01 to 300 mm/h and divided into 50 bins.

3.3.5. Latitudinal Distribution Analysis

Figure 12a–c shows the latitudinal zonal distribution of precipitation based on the coincident precipitation events in Groups 1 and 2, respectively. Three peaks are clearly presented in the curves in Figure 12a, while more peaks exist in Figure 12b. This is partly due to the fact that the sample size of Group 2 is smaller. To provide a more reliable and sufficient analysis, the latitudinal distribution of precipitation based on Group 3 is calculated, as presented in Figure 12c. Although GPM DPR captures much more light precipitation events than TRMM PR, the total precipitation volume of the coincident events derived by the two radars is relatively close, with the two solid curves almost overlapping. Two peaks of the total precipitation volume appear near the middle latitude zones (around 35°N/S). However, around 30°S, the total precipitation volume, as well as stratiform and convective precipitation volume, detected by GPM DPR exceeded that of TRMM PR significantly in Figure 12a,c, while, in Figure 12b, the total precipitation volume detected by TRMM PR and GPM DPR is very close. In regions around 3°S, the situation reverses. Therefore, we further computed the fraction of the two rain types at each latitude, which is the precipitation volume of a certain rain type divided by the total precipitation volume. The histograms of accumulated precipitation based on coincident events in Groups 2 and 3 in these abnormal regions are calculated to explore the causes.

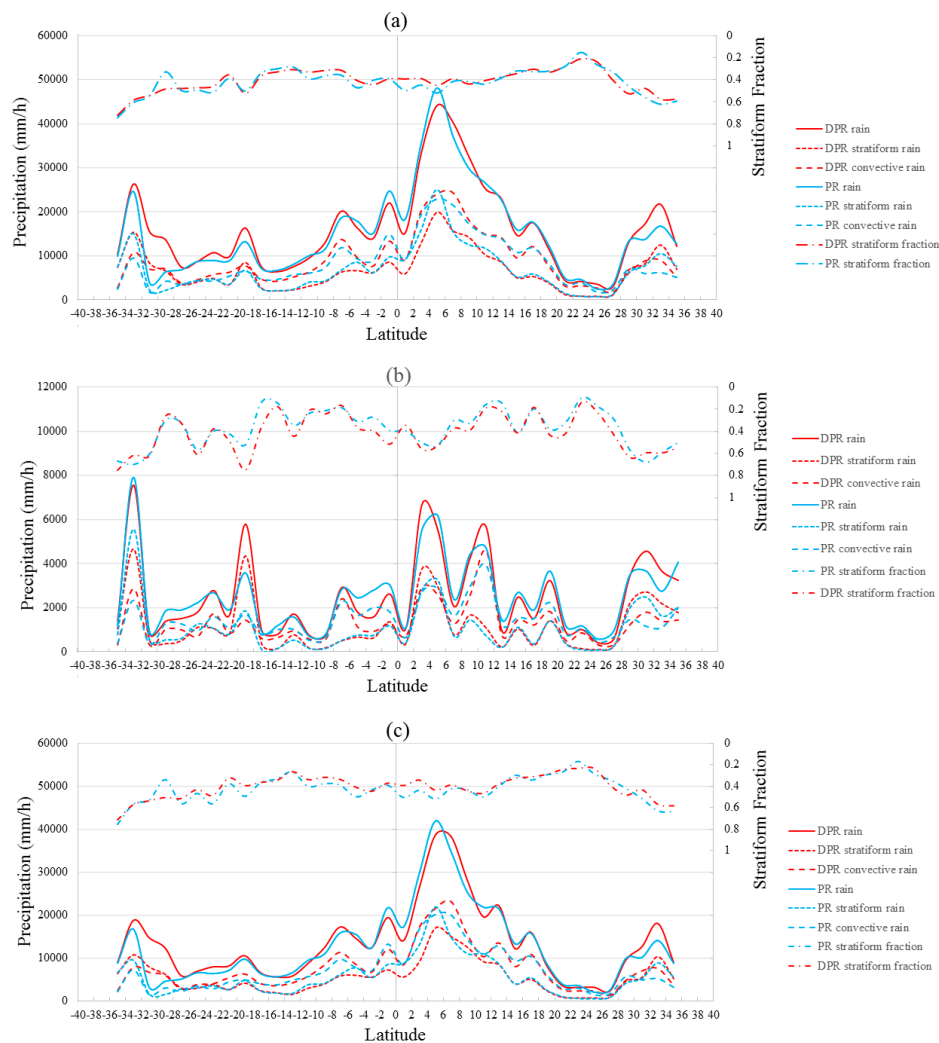


Figure 12. Cont.

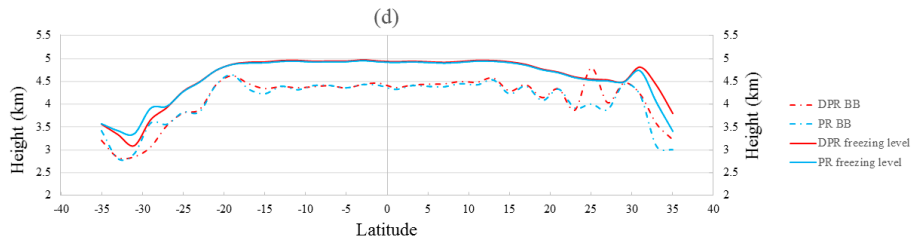


Figure 12. The latitudinal zonal distribution map for: (a–c) precipitation; and (d) height of freezing level and BB based on the coincident events. Panels (a,d) are based on the coincident events in Group 1; Panel (b) is based on Group 2; and Panel (c) is based on Group 3. All data are resampled to a spatial resolution of 2°.

In Figure 13a, regardless of the magnitude of rain rates, the accumulated volume of precipitation detected by GPM DPR largely exceeded that of TRMM PR in Group 3, especially for precipitation with rain rates between 1 and 10 mm/h. Moreover, the fraction of stratiform precipitation detected by GPM DPR was much higher than that of TRMM PR around 30°S in the outer swath. This indicates that in regions around 30°S, GPM DPR detects more stratiform precipitation than TRMM PR mainly in the outer swath. For regions around 3°S, Figure 13b shows that both inner and outer swath of TRMM PR detect more precipitation with rain rates between 1 and 10 mm/h, particularly for inner swath. It is noted that the extra precipitation captured by TRMM PR was mainly convective.

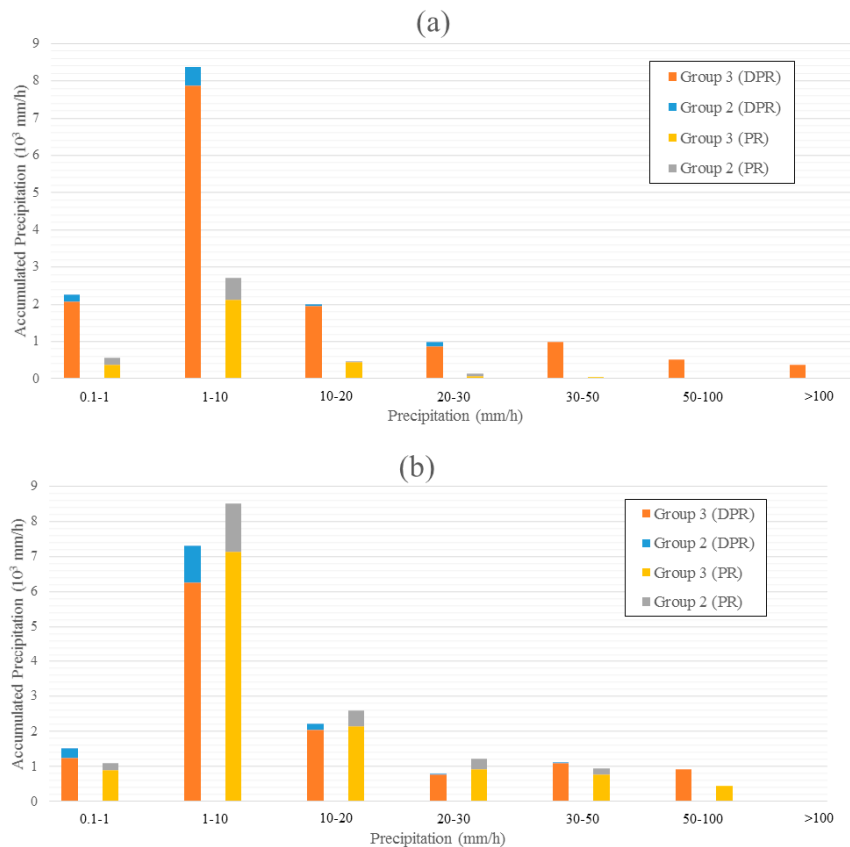


Figure 13. Cont.

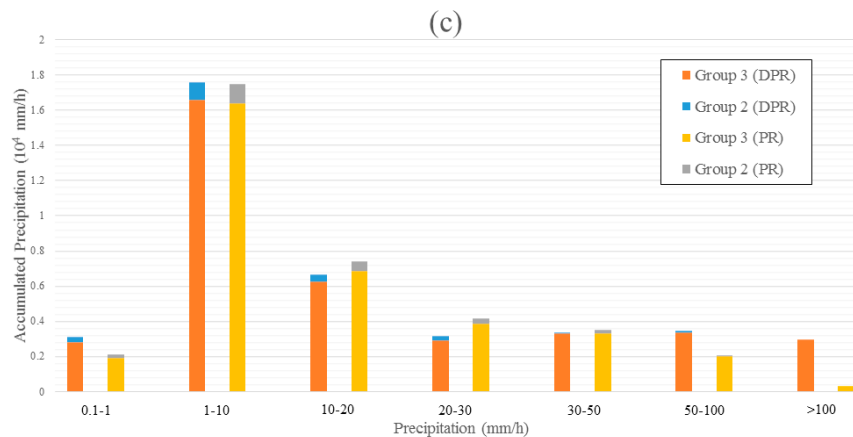


Figure 13. Histograms of accumulated precipitation based on coincident events between DPR and PR in Group 2 and 3: (a) coincident events occurring between 30°S and 32°S; (b) coincident events occurring between 2°S and 4°S; and (c) coincident events occurring between 6°N and 8°N.

It is noticed that around 7°N, the solid curves of both GPM DPR and TRMM PR in Figure 12b show abnormal troughs compared to Figure 12a,c. Figure 13c shows that precipitation with rain rates higher than 30 mm/h is very rare in Group 2. This is because more heavy precipitation, which was mainly distributed in the Amazon rainforest, was captured in the outer swath.

We also discovered that both stratiform and convective precipitation appear to have the same quantitative characteristics, with stratiform precipitation making up a relatively significant share of the total precipitation volume in the regions with latitudes higher than 20°N or 30°S.

Figure 12d presents the latitudinal zonal distribution map of averaged freezing level height and averaged BB height based on the coincident events in Group 1. In regions between 20°N/S, the freezing level height of TRMM PR and GPM DPR remained almost the same at about 5 km, and the BB height fluctuated just 500 m below the freezing level. Thurai and Iguchi [75] discovered that between 15°N/S, the BB heights were between 4 and 4.5 km, using TRMM PR's two-year data. As the latitude exceeded 30°N and 20°S, the freezing level height and BB height decreased sharply. Thurai et al. [76] found that both BB height and freezing level height are latitudinally dependent. By applying both 4-year TRMM PR's observation and the averaged ITU-R Recommendation P.839-3, they noted that in regions between 20°N/S and 30°N/S, both heights decreased from above 4 km to around 3 km. However, the estimates of freezing level height produced by TRMM PR and GPM PR on the coincident events had some small discrepancies. Around 30°N, GPM DPR's estimate was a little higher than that of PR, and this situation was reversed around 30°S. This is consistent with the result shown in Figure 5c. The heights of both freezing level and BB rose again in regions near 37°S. These discrepancies and unexpected increases in height may be attributed to the limited sample size. Since the detection of BB is done within a search window whose center was about 0.5 km below the freezing level, and just exactly the freezing level for GPM DPR and TRMM PR, respectively [26,40], the trend for the distribution curves of averaged BB height of the two radars corresponded well with those curves of averaged freezing level height. However, around 25°N, speaking of GPM DPR, the curve of averaged BB height was higher than that of averaged freezing level height. This phenomenon may be caused by the two radars' relatively coarse range resolution of 250 m, which can lead to a large variation of BB height [41], making it difficult to precisely determine the BB height in these regions [41]. In higher latitudes, the difference between freezing level height and BB height increased. This indicates that the melting layer thickness is latitude dependent [76].

4. Conclusions and Outlook

Since the TRMM has been providing essential data for nearly 17 years and terminated operation in 2015, the GPM is expected to inherit the legacy and further improve global precipitation measurement. This study aimed to explore the similarities and improvements in precipitation rate estimates, type classification and vertical profiling provided by the two missions. Therefore, direct comparisons between TRMM PR and GPM DPR were conducted in the overlapping period. We not only matched the whole swath data of both the two radars as Group 1, but also matched only the inner 25 beams' data of them as Group 2, and Group 3 was obtained by excluding Group 2 from Group 1. The comparison was mainly focused on rain type classification and detection. We employed the level 2 product TRMM 2A23, 2A25 and GPM 2ADPR to conduct the direct comparison over the overlapping period. The major conclusions of this study are as follows:

1. Generally speaking, GPM DPR and TRMM PR correspond well with each other in estimating both the intensity and distribution of precipitation globally. GPM DPR is much more sensitive at detecting light precipitation by improving the KuPR's sensitivity and combining the observation of KaPR with the traditional KuPR, compared with TRMM single Ku-band PR. At the coincident events obtained in both whole swath data and the inner beams, the occurrences of all kinds of precipitation and light precipitation (rain rates < 1 mm/h) detected by DPR were ~1.7 and ~2.53 times more than that of PR. However, when precipitation events were captured by both radars, TRMM PR tended to give a higher estimation of precipitation rates for rates between 0.6 and 3 mm/h.
2. GPM DPR gives a slight overestimation of freezing level height in the tropical regions, while in the middle latitudes its estimate of freezing level height is lower than that of TRMM PR. The difference between the estimates of freezing level given by the two radars was within ± 100 m at low latitudes. The observations of BB height were in general consistency with that of freezing level height, though in some regions the difference between the two heights was up to 1 km. According to comparisons of coincident events in all swath data, the correlation coefficients of freezing level height and BB height between the two radars were 0.997 and 0.947, respectively.
3. GPM DPR distinguishes rain types more clearly and classifies more precipitation events as "stratiform" and "convective" with no precipitation events classified as "missing". DPR reduces the misclassification of clouds and noise signals as precipitation type "other" (from 10.14%) to 0.51% for all swath data. DFRm decision for rain type classification was close to that of Ku-only method decision. In the inner swath and outer swath of DPR, the results were consistent. Around 82.89% of "stratiform" precipitation recognized by PR was classified into "stratiform" by DPR. The consistency of classification of convective precipitation between DPR and PR was a little worse than that of stratiform precipitation, as 71.02% of PR's convective precipitation was regarded the same in DPR.
4. Regardless of the types of the earth's surface, GPM DPR detects more precipitation than TRMM PR. However, TRMM PR developed a slight trend in detecting more precipitation than GPM DPR when the rainfall rate increases to exceed 1 mm/h, particularly over coast and land. The performance of the two radars was quite close over the ocean. Further study needs to be conducted over complex mountainous terrain.
5. Although GPM DPR captured significantly more light precipitation events than TRMM PR, the distribution of total precipitation volume of the coincident events derived by the two radars was relatively close, regardless of precipitation types. Both freezing level height and BB height showed obvious latitudinal dependence. However, for regions near 30°N/S, the estimates of freezing level height produced by TRMM PR and GPM PR were discrepant while estimates of BB height agreed well with each other.

These results are expected to further improve the algorithm for spaceborne radars and provide a deeper understanding of the global organized precipitation systems for researchers. However, in this

study, the relationship between the precipitation and the topography was not considered due to current page limits. Furthermore, because the atmospheric environment changes as the climate zone changes, and the vertical profile of radar equivalent reflectivity is seriously affected by the atmospheric conditions, further investigations comparing the performances of the two radars in different climate zones are needed. To gain a deep understanding of this subject, data obtained from rain gauges and ground-based radars in different areas may be required to fill the data gap, which would then allow for an investigation into GPM DPR's accuracy.

As for the prospects of spaceborne precipitation radars, there is no doubt that they will continue to be of vital importance in research. By improving radar's detectability and adding another band to obtain more information, GPM DPR has proved to be a more advanced instrument than TRMM PR. However, attention should be paid to the fact that high frequency radar sensors often encounter problems of significant attenuation in heavy precipitation events [77]. In addition, since the specific methods adopted to adjust the attenuation have strong assumptions, they can have a profound effect on the quality of the final precipitation estimates. Combining sensors operating at other frequencies to obtain more detailed information to enhance the estimation of precipitation with different intensities and phases is an effective way to solve this problem [29]. Other efforts such as the constructing constellation of various instruments and platforms can make a great contribution as well. NASA's Jet Propulsion Laboratory's (JPL's) new mission, RainCube, takes advantages of a number of CubeSat satellites and pairs of low-cost Ka band radar system to achieve a more frequent earth observation with higher temporal and spatial resolution [78,79]. Allamano et al. have explored the use of mobile video and imagery to capture and analyze precipitation events, showing that crowd-source projects have a promising future in earth observation [79,80].

Acknowledgments: This study was financially supported by the National Natural Science Foundation of China (Grant No. 71461010701 and 91437214) and China-USA CERC 2016YFE0102400. The authors are grateful for JAXA and NASA, for providing the TRMM and GPM observation datasets. TRMM 2A23 and 2A25 version 7 data are available at the Goddard Earth Sciences Data and Information Services Center, National Aeronautics and Space Administration; GPM version 04A 2ADPR data are available at the Precipitation Processing System, National Aeronautics and Space Administration Goddard Space Flight Center. We also appreciate Associate Professor Di Long for their valuable comments on revising the manuscript.

Author Contributions: Jinyu Gao analyzed the data and prepared the draft of the manuscript. Guoqiang Tang prepared the satellite precipitation data and revised the manuscript. Yang Hong conceived this study, gave comments and significantly revised the manuscript.

Conflicts of Interest: The authors declare no conflict of interest. The founding sponsors had no role in the design of the study; in the collection, analyses, or interpretation of data; in the writing of the manuscript, and in the decision to publish the results.

References

1. Schouppé, M.; Ghazi, A. European Commission Research for Global Climate Change Studies: Towards Improved Water Observations and Forecasting Capability. In *Measuring Precipitation from Space*; Springer: Dordrecht, The Netherlands, 2007; pp. 3–6.
2. Ebert, E.E.; Janowiak, J.E.; Kidd, C. Comparison of near-real-time precipitation estimates from satellite observations and numerical models. *Bull. Am. Meteorol. Soc.* **2007**, *88*, 47–64. [[CrossRef](#)]
3. Ma, Y.; Zhang, Y.; Yang, D.; Farhan, S.B. Precipitation bias variability versus various gauges under different climatic conditions over the Third Pole Environment (TPE) region. *Int. J. Climatol.* **2015**, *35*, 1201–1211. [[CrossRef](#)]
4. Sorooshian, S.; AghaKouchak, A.; Arkin, P.; Eylander, J.; Fofoula-Georgiou, E.; Harmon, R.; Hendrickx, J.M.; Imam, B.; Kuligowski, R.; Skahill, B. Advancing the remote sensing of precipitation. *Bull. Am. Meteorol. Soc.* **2011**, *92*, 1271–1272. [[CrossRef](#)]
5. Hou, A.Y.; Kakar, R.K.; Neeck, S.; Azarbarzin, A.A.; Kummerow, C.D.; Kojima, M.; Oki, R.; Nakamura, K.; Iguchi, T. The global precipitation measurement mission. *Bull. Am. Meteorol. Soc.* **2014**, *95*, 701–722. [[CrossRef](#)]

6. Bellerby, T.; Todd, M.; Kniveton, D.; Kidd, C. Rainfall estimation from a combination of TRMM precipitation radar and GOES multispectral satellite imagery through the use of an artificial neural network. *J. Appl. Meteorol.* **2000**, *39*, 2115–2128. [[CrossRef](#)]
7. Kidd, C.; Kniveton, D.R.; Todd, M.C.; Bellerby, T.J. Satellite rainfall estimation using combined passive microwave and infrared algorithms. *J. Hydrometeorol.* **2003**, *4*, 1088–1104. [[CrossRef](#)]
8. Kidd, C.; Bauer, P.; Turk, J.; Huffman, G.; Joyce, R.; Hsu, K.-L.; Braithwaite, D. Intercomparison of high-resolution precipitation products over Northwest Europe. *J. Hydrometeorol.* **2012**, *13*, 67–83. [[CrossRef](#)]
9. Hossain, F.; Lettenmaier, D.P. Flood prediction in the future: Recognizing hydrologic issues in anticipation of the Global Precipitation Measurement mission. *Water Resour. Res.* **2006**, *42*. [[CrossRef](#)]
10. Kidd, C.; Levizzani, V. Status of satellite precipitation retrievals. *Hydrol. Earth Syst. Sci.* **2011**, *15*, 1109–1116. [[CrossRef](#)]
11. Iguchi, T.; Oki, R.; Smith, E.; Furuhashi, Y. Global Precipitation Measurement program and the development of dual-frequency precipitation radar. *J. Commun. Res. Lab.* **2002**, *49*, 37–46.
12. Kummerow, C.; Simpson, J.; Thiele, O.; Barnes, W.; Chang, A.; Stocker, E.; Adler, R.; Hou, A.; Kakar, R.; Wentz, F. The status of the Tropical Rainfall Measuring Mission (TRMM) after two years in orbit. *J. Appl. Meteorol.* **2000**, *39*, 1965–1982. [[CrossRef](#)]
13. Rui, L.; Yunfei, F. Tropical precipitation estimated by GPCP and TRMM PR observations. *Adv. Atmos. Sci.* **2005**, *22*, 852–864. [[CrossRef](#)]
14. Seto, S.; Iguchi, T. Rainfall-induced changes in actual surface backscattering cross sections and effects on rain-rate estimates by spaceborne precipitation radar. *J. Atmos. Ocean. Technol.* **2007**, *24*, 1693–1709. [[CrossRef](#)]
15. Amitai, E.; Lloret, X.; Sempere-Torres, D. Comparison of TRMM radar rainfall estimates with NOAA next-generation QPE. *J. Meteorol. Soc. Jpn. Ser. II* **2009**, *87*, 109–118. [[CrossRef](#)]
16. Kirstetter, P.-E.; Hong, Y.; Gourley, J.J.; Chen, S.; Flamig, Z.; Zhang, J.; Schwaller, M.; Petersen, W.; Amitai, E. Toward a Framework for Systematic Error Modeling of Spaceborne Precipitation Radar with NOAA/NSSL Ground Radar-Based National Mosaic QPE. *J. Hydrometeorol.* **2012**, *13*, 1285–1300. [[CrossRef](#)]
17. Liao, L.; Meneghini, R.; Iguchi, T. Comparisons of rain rate and reflectivity factor derived from the TRMM precipitation radar and the WSR-88D over the Melbourne, Florida, site. *J. Atmos. Ocean. Technol.* **2001**, *18*, 1959–1974. [[CrossRef](#)]
18. Wang, J.; Wolff, D.B. Comparisons of Reflectivities from the TRMM Precipitation Radar and Ground-Based Radars. *J. Atmos. Ocean. Technol.* **2009**, *26*, 857–875. [[CrossRef](#)]
19. Bolen, S.M.; Chandrasekar, V. Quantitative cross validation of space-based and ground-based radar observations. *J. Appl. Meteorol.* **2000**, *39*, 2071–2079. [[CrossRef](#)]
20. Kirstetter, P.-E.; Hong, Y.; Gourley, J.; Schwaller, M.; Petersen, W.; Zhang, J. Comparison of trmm 2A25 products, version 6 and version 7, with NOAA/NSSL ground radar-based national mosaic QPE. *J. Hydrometeorol.* **2013**, *14*, 661–669. [[CrossRef](#)]
21. Masunaga, H.; Iguchi, T.; Oki, R.; Kachi, M. Comparison of rainfall products derived from TRMM microwave imager and precipitation radar. *J. Appl. Meteorol.* **2002**, *41*, 849–862. [[CrossRef](#)]
22. Liao, L.; Meneghini, R. Validation of TRMM precipitation radar through comparison of its multiyear measurements with ground-based radar. *J. Appl. Meteorol. Climatol.* **2009**, *48*, 804–817. [[CrossRef](#)]
23. Anagnostou, E.N.; Morales, C.A.; Dinku, T. The Use of TRMM Precipitation Radar Observations in Determining Ground Radar Calibration Biases. *J. Atmos. Ocean. Technol.* **2001**, *18*, 616–628. [[CrossRef](#)]
24. Zhong, L.; Yang, R.; Wen, Y.; Chen, L.; Gou, Y.; Li, R.; Zhou, Q.; Hong, Y. Cross-evaluation of reflectivity from the space-borne precipitation radar and multi-type ground-based weather radar network in China. *Atmos. Res.* **2017**, *196*, 200–210. [[CrossRef](#)]
25. Saraiva, I.; Silva Dias, M.; Morales, C.; Saraiva, J. Regional Variability of Rain Clouds in the Amazon Basin as Seen by a Network of Weather Radars. *J. Appl. Meteorol. Climatol.* **2016**, *55*, 2657–2675. [[CrossRef](#)]
26. Awaka, J.; Iguchi, T.; Okamoto, K. TRMM PR standard algorithm 2A23 and its performance on bright band detection. *J. Meteorol. Soc. Jpn. Ser. II* **2009**, *87*, 31–52. [[CrossRef](#)]
27. Hamada, A.; Takayabu, Y.N.; Liu, C.; Zipser, E.J. Weak linkage between the heaviest rainfall and tallest storms. *Nat. Commun.* **2015**, *6*. [[CrossRef](#)] [[PubMed](#)]

28. Hamada, A.; Takayabu, Y.N. Improvements in detection of light precipitation with the Global Precipitation measurement dual-frequency precipitation radar (GPM DPR). *J. Atmos. Ocean. Technol.* **2016**, *33*, 653–667. [[CrossRef](#)]
29. Tang, G.; Wen, Y.; Gao, J.; Long, D.; Ma, Y.; Wan, W.; Hong, Y. Similarities and differences between three coexisting spaceborne radars in global rainfall and snowfall estimation. *Water Resour. Res.* **2017**. [[CrossRef](#)]
30. Ma, Y.; Tang, G.; Long, D.; Yong, B.; Zhong, L.; Wan, W.; Hong, Y. Similarity and error intercomparison of the GPM and its predecessor-TRMM Multisatellite Precipitation Analysis using the best available hourly gauge network over the Tibetan Plateau. *Remote Sens.* **2016**, *8*, 569. [[CrossRef](#)]
31. Dinku, T.; Ceccato, P.; Connor, S.J. Challenges of satellite rainfall estimation over mountainous and arid parts of east Africa. *Int. J. Remote Sens.* **2011**, *32*, 5965–5979. [[CrossRef](#)]
32. Tian, Y.; Peters-Lidard, C.D. A global map of uncertainties in satellite-based precipitation measurements. *Geophys. Res. Lett.* **2010**, *37*. [[CrossRef](#)]
33. Su, F.; Hong, Y.; Lettenmaier, D.P. Evaluation of TRMM Multisatellite Precipitation Analysis (TMPA) and its utility in hydrologic prediction in the La Plata Basin. *J. Hydrometeorol.* **2008**, *9*, 622–640. [[CrossRef](#)]
34. Huffman, G.J.; Bolvin, D.T.; Nelkin, E.J.; Wolff, D.B.; Adler, R.F.; Gu, G.; Hong, Y.; Bowman, K.P.; Stocker, E.F. The TRMM multisatellite precipitation analysis (TMPA): Quasi-global, multiyear, combined-sensor precipitation estimates at fine scales. *J. Hydrometeorol.* **2007**, *8*, 38–55. [[CrossRef](#)]
35. Beck, H.E.; Vergopolan, N.; Pan, M.; Levizzani, V.; van Dijk, A.I.; Weedon, G.; Brocca, L.; Pappenberger, F.; Huffman, G.J.; Wood, E.F. Global-Scale Evaluation of 23 Precipitation Datasets Using Gauge Observations and Hydrological modeling. *Hydrol. Earth Syst. Sci.* **2017**. [[CrossRef](#)]
36. Huffman, G.J.; Bolvin, D.T.; Braithwaite, D.; Hsu, K.; Joyce, R.; Xie, P.; Yoo, S.-H. NASA global precipitation measurement (GPM) integrated multi-satellite retrievals for GPM (IMERG). In *Algorithm Theoretical Basis Document (ATBD)*; NASA/GSFC: Greenbelt, MD, USA, 2014.
37. Houze, R.A.; Hobbs, P.V. Organization and structure of precipitating cloud systems. *Adv. Geophys.* **1982**, *24*, 225–315.
38. Houze, R.A. Observed structure of mesoscale convective systems and implications for large-scale heating. *Q. J. R. Meteorol. Soc.* **1989**, *115*, 425–461. [[CrossRef](#)]
39. Robert, A. Cloud clusters and large-scale vertical motions in the tropics. *J. Meteorol. Soc. Jpn. Ser. II* **1982**, *60*, 396–410.
40. Iguchi, T.; Seto, S.; Meneghini, R.; Yoshida, N.; Awaka, J.; Kubota, T. *GPM/DPR Level-2 Algorithm Theoretical Basis Document*; Technical Report; NASA Goddard Space Flight Center: Greenbelt, MD, USA, 2010.
41. Team, T.P.R. *Tropical Rainfall Measuring Mission (TRMM) Precipitation Radar Algorithm: Instruction Manual for Version 7*; Japan Aerospace Exploration Agency: Tokyo, Japan, 2011.
42. Haddad, Z.S.; Smith, E.A.; Kummerow, C.D.; Iguchi, T.; Farrar, M.R.; Durden, S.L.; Alves, M.; Olson, W.S. The TRMM ‘day-1’ radar/radiometer combined rain-profiling algorithm. *J. Meteorol. Soc. Jpn. Ser. II* **1997**, *75*, 799–809. [[CrossRef](#)]
43. Awaka, J.; Iguchi, T.; Okamoto, K. Rain type classification algorithm. In *Measuring Precipitation from Space*; Springer: Dordrecht, The Netherlands, 2007; pp. 213–224.
44. Schumacher, C.; Houze, R.A., Jr. Stratiform rain in the tropics as seen by the TRMM precipitation radar. *J. Clim.* **2003**, *16*, 1739–1756. [[CrossRef](#)]
45. Yang, S.; Smith, E.A. Convective–Stratiform Precipitation Variability at Seasonal Scale from 8 Yr of TRMM Observations: Implications for Multiple Modes of Diurnal Variability. *J. Clim.* **2008**, *21*, 4087–4114. [[CrossRef](#)]
46. Houze, R.A., Jr. Stratiform precipitation in regions of convection: A meteorological paradox? *Bull. Am. Meteorol. Soc.* **1997**, *78*, 2179–2196. [[CrossRef](#)]
47. Awaka, J.; Iguchi, T.; Kumagai, H.; Okamoto, K. Rain type classification algorithm for TRMM precipitation radar. In *Proceedings of the IEEE International Geoscience and Remote Sensing, 1997. Remote Sensing-A Scientific Vision for Sustainable Development, Singapore, 3–8 August 1997*; pp. 1633–1635.
48. Steiner, M.; Houze, R.A., Jr.; Yuter, S.E. Climatological characterization of three-dimensional storm structure from operational radar and rain gauge data. *J. Appl. Meteorol.* **1995**, *34*, 1978–2007. [[CrossRef](#)]
49. Iguchi, T.; Kozu, T.; Meneghini, R.; Awaka, J.; Okamoto, K. Rain-profiling algorithm for the TRMM precipitation radar. *J. Appl. Meteorol.* **2000**, *39*, 2038–2052. [[CrossRef](#)]
50. Shrestha, D.; Singh, P.; Nakamura, K. Spatiotemporal variation of rainfall over the central Himalayan region revealed by TRMM Precipitation Radar. *J. Geophys. Res. Atmos.* **2012**, *117*. [[CrossRef](#)]

51. Le, M.; Chandrasekar, V. Precipitation type classification method for dual-frequency precipitation radar (DPR) onboard the GPM. *IEEE Trans. Geosci. Remote Sens.* **2013**, *51*, 1784–1790. [[CrossRef](#)]
52. Awaka, J.; Le, M.; Chandrasekar, V.; Yoshida, N.; Higashiawatoko, T.; Kubota, T.; Iguchi, T. Rain Type Classification Algorithm Module for GPM Dual-Frequency Precipitation Radar. *J. Atmos. Ocean. Technol.* **2016**, *33*, 1887–1898. [[CrossRef](#)]
53. Hirose, M.; Shimizu, S.; Oki, R.; Iguchi, T.; Short, D.A.; Nakamura, K. Incidence-Angle Dependency of TRMM PR Rain Estimates. *J. Atmos. Ocean. Technol.* **2012**, *29*, 192–206. [[CrossRef](#)]
54. Kubota, T.; Iguchi, T.; Kojima, M.; Liao, L.; Masaki, T.; Hanado, H.; Meneghini, R.; Oki, R. A Statistical Method for Reducing Sidelobe Clutter for the Ku-Band Precipitation Radar on board the GPM Core Observatory. *J. Atmos. Ocean. Technol.* **2016**, *33*, 1413–1428. [[CrossRef](#)]
55. Kelley, O.A. Where the least rainfall occurs in the Sahara Desert, the TRMM radar reveals a different pattern of rainfall each season. *J. Clim.* **2014**, *27*, 6919–6939. [[CrossRef](#)]
56. Iguchi, T.; Seto, S.; Awaka, J.; Meneghini, R.; Kubota, T.; Chandra, V.; Yoshida, N.; Kawamoto, N.; Oki, R. Precipitation rates estimated with GPM's Dual-frequency Radar. In Proceedings of the 2016 IEEE International Geoscience and Remote Sensing Symposium (IGARSS), Beijing, China, 10–15 July 2016; pp. 3917–3918.
57. Funk, A.; Schumacher, C.; Awaka, J. Analysis of rain classifications over the tropics by version 7 of the TRMM PR 2A23 algorithm. *J. Meteorol. Soc. Jpn. Ser. II* **2013**, *91*, 257–272. [[CrossRef](#)]
58. Schumacher, C.; Houze, R.A., Jr. The TRMM precipitation radar's view of shallow, isolated rain. *J. Appl. Meteorol.* **2003**, *42*, 1519–1524. [[CrossRef](#)]
59. Fu, Y.; Feng, S.; Liu, P.; Cao, A.; Liu, X.; Li, R.; Liu, Q.; Wang, Y. The cumulonimbus incus in summer Asia as detected by the TRMM PR. *Acta Meteorol. Sin.* **2010**, *2*, 195–206.
60. Shimizu, S.; Oki, R.; Tagawa, T.; Iguchi, T.; Hirose, M. Evaluation of the Effects of the Orbit Boost of the TRMM Satellite on PR Rain Estimates. *J. Meteorol. Soc. Jpn. Ser. II* **2009**, *87A*, 83–92. [[CrossRef](#)]
61. Liu, X.T.; Fu, Y.F.; Liu, Q. Significant impacts of the TRMM satellite orbit boost on climatological records of tropical precipitation. *Chin. Sci. Bull.* **2012**, *57*, 4627–4634. [[CrossRef](#)]
62. Liang, L.; Meneghini, R. Changes in the TRMM version-5 and version-6 precipitation radar products due to orbit boost. *J. Meteorol. Soc. Jpn. Ser. II* **2009**, *87*, 93–107.
63. Nakazawa, T.; Rajendran, K. Interannual variability of tropical rainfall characteristics and the impact of the altitude boost from TRMM PR 3A25 data. *J. Meteorol. Soc. Jpn. Ser. II* **2009**, *87*, 317–338. [[CrossRef](#)]
64. Kojima, M.; Miura, T.; Furukawa, K.; Hyakusoku, Y.; Ishikiri, T.; Kai, H.; Iguchi, T.; Hanado, H.; Nakagawa, K. Dual-frequency precipitation radar (DPR) development on the global precipitation measurement (GPM) core observatory. *Proc. SPIE* **2012**, *8528*. [[CrossRef](#)]
65. Toyoshima, K.; Masunaga, H.; Furuzawa, F.A. Early Evaluation of Ku- and Ka-Band Sensitivities for the Global Precipitation Measurement (GPM) Dual-Frequency Precipitation Radar (DPR). *Sola* **2015**, *11*, 14–17. [[CrossRef](#)]
66. Bolen, S.M.; Chandrasekar, V. Methodology for aligning and comparing spaceborne radar and ground-based radar observations. *J. Atmos. Ocean. Technol.* **2003**, *20*, 647–659. [[CrossRef](#)]
67. Schumacher, C.; Houze, R.A., Jr. Comparison of Radar Data from the TRMM Satellite and Kwajalein Oceanic Validation Site. *J. Appl. Meteorol.* **2000**, *39*, 2151–2164. [[CrossRef](#)]
68. Ikai, J.; Nakamura, K. Comparison of rain rates over the ocean derived from TRMM microwave imager and precipitation radar. *J. Atmos. Ocean. Technol.* **2003**, *20*, 1709–1726. [[CrossRef](#)]
69. Kim, J.-H.; Ou, M.-L.; Park, J.-D.; Morris, K.R.; Schwaller, M.R.; Wolff, D.B. Global precipitation measurement (GPM) ground validation (GV) prototype in the Korean Peninsula. *J. Atmos. Ocean. Technol.* **2014**, *31*, 1902–1921. [[CrossRef](#)]
70. Chen, S.; Kirstetter, P.; Hong, Y.; Gourley, J.; Tian, Y.; Qi, Y.; Cao, Q.; Zhang, J.; Howard, K.; Hu, J. Evaluation of spatial errors of precipitation rates and types from TRMM spaceborne radar over the southern CONUS. *J. Hydrometeorol.* **2013**, *14*, 1884–1896. [[CrossRef](#)]
71. Kubota, T.; Yoshida, N.; Urita, S.; Iguchi, T.; Seto, S.; Meneghini, R.; Awaka, J.; Hanado, H.; Kida, S.; Oki, R. Evaluation of precipitation estimates by at-launch codes of GPM/DPR algorithms using synthetic data from TRMM/PR observations. *IEEE J. Sel. Top. Appl. Earth Obs. Remote Sens.* **2014**, *7*, 3931–3944. [[CrossRef](#)]
72. Le, M.; Chandrasekar, V.; Biswas, S. Evaluation and Validation of GPM Dual-Frequency Classification Module after Launch. *J. Atmos. Ocean. Technol.* **2016**, *33*, 2699–2716. [[CrossRef](#)]

73. Qing, H.; Chu, Y.; Zhao, Z.; Su, C.; Zhou, C.; Zhang, Y. Observation and analysis of atmospheric rainfall based on the very high frequency radar. *IET Radar Sonar Navig.* **2016**, *11*, 616–620. [[CrossRef](#)]
74. Heymsfield, G.M.; Tian, L.; Li, L.; McLinden, M.; Cervantes, J.I. Airborne radar observations of severe hailstorms: Implications for future spaceborne radar. *J. Appl. Meteorol. Climatol.* **2013**, *52*, 1851–1867. [[CrossRef](#)]
75. Thurai, M.; Iguchi, T. Rain height information from TRMM precipitation radar. *Electron. Lett.* **2000**, *36*, 1059–1061. [[CrossRef](#)]
76. Thurai, M.; Deguchi, E.; Iguchi, T.; Okamoto, K. Freezing height distribution in the tropics. *Int. J. Satell. Commun. Netw.* **2003**, *21*, 533–545. [[CrossRef](#)]
77. Meneghini, R.; Kim, H.; Liao, L.; Jones, J.A.; Kwiatkowski, J.M. An initial assessment of the surface reference technique applied to data from the Dual-Frequency Precipitation Radar (DPR) on the GPM satellite. *J. Atmos. Ocean. Technol.* **2015**, *32*, 2281–2296. [[CrossRef](#)]
78. Haddada, Z.S.; Perala, E.; Tanellia, S.; Sya, O.; Stephensa, G. RaInCube: A proposed constellation of atmospheric profiling radars in cubesat. *SPIE Asia-Pac. Remote Sens. Int. Soc. Opt. Photonics* **2016**, 9876. [[CrossRef](#)]
79. McCabe, M.F.; Rodell, M.; Alsdorf, D.E.; Miralles, D.G.; Uijlenhoet, R.; Wagner, W.; Lucieer, A.; Houborg, R.; Verhoest, N.E.; Franz, T.E. The future of earth observation in hydrology. *Hydrol. Earth Syst. Sci* **2017**, *21*, 3879–3914. [[CrossRef](#)]
80. Allamano, P.; Croci, A.; Laio, F. Toward the camera rain gauge. *Water Resour. Res.* **2015**, *51*, 1744–1757. [[CrossRef](#)]



© 2017 by the authors. Licensee MDPI, Basel, Switzerland. This article is an open access article distributed under the terms and conditions of the Creative Commons Attribution (CC BY) license (<http://creativecommons.org/licenses/by/4.0/>).